석사 학위논문
Master's Thesis

가변적 액정 필터를 이용한 두 방향 초분광 이미징 시스템의 개발

Building a Two-Way Hyperspectral Imaging System with Liquid Crystal Tunable Filters

이 해 봄 (李 해 봄 Lee, Hae Bom)
전산학부
School of Computing

KAIST

2015

가변적 액정 필터를 이용한 두 방향 초분광 이미징 시스템의 개발

Building a Two-Way Hyperspectral Imaging System with Liquid Crystal Tunable Filters

Building a Two-Way Hyperspectral Imaging System with Liquid Crystal Tunable Filters

Advisor : Professor Kim, Min Hyuk

by
Lee, Hae Bom
School of Computing
KAIST

A thesis submitted to the faculty of KAIST in partial fulfillment of the requirements for the degree of Master of Science and Engineering in the School of Computing . The study was conducted in accordance with Code of Research Ethics[1].

2015. 6. 22.

Approved by

Professor Kim, Min Hyuk

[Advisor]

---

[1]Declaration of Ethical Conduct in Research: I, as a graduate student of KAIST, hereby declare that I have not committed any acts that may damage the credibility of my research. These include, but are not limited to: falsification, thesis written by someone else, distortion of research findings or plagiarism. I affirm that my thesis contains honest conclusions based on my own careful research under the guidance of my thesis advisor.

가변적 액정 필터를 이용한 두 방향 초분광 이미징 시스템의 개발

이 해 봄

위 논문은 한국과학기술원 석사학위논문으로
학위논문심사위원회에서 심사 통과하였음.

2015년 6월 22일

심사위원장 김 민 혁 (인)

심사위원 박 진 아 (인)

심사위원 윤 성 의 (인)

MCS
20134588

이 해 봄. Lee, Hae Bom. Building a Two-Way Hyperspectral Imaging System with Liquid Crystal Tunable Filters. 가변적 액정 필터를 이용한 두 방향 초분광 이미징 시스템의 개발. School of Computing . 2015. 47p. Advisor Prof. Kim, Min Hyuk. Text in English.

ABSTRACT

Liquid crystal tunable filters can provide rapid and vibrationless section of any wavelength in transmitting spectrum so that they have been broadly used in building multispectral or hyperspectral imaging systems. However, the spectral range of the filters is limited to a certain range, such as visible or near-infrared spectrum. In general hyperspectral imaging applications, we are therefore forced to choose a certain range of target spectrum, either visible or near-infrared for instance. Owing to the nature of polarizing optical elements, imaging systems combined with multiple tunable filters have been rarely practiced. In this paper, we therefore present our experience of building a two-way hyperspectral imaging system with liquid crystal tunable filters. The system allows us to capture hyperspectral radiance continuously from visible to near-infrared spectrum (400—1100 nm at 7 nm intervals), which is 2.3 times wider and 34 times more channels compared to a common RGB camera. We report how we handle the multiple polarizing elements to extend the spectral range of the imager with the multiple tunable filters and propose an affine-based method to register the hyperspectral image channels of each wavelength.

Contents

List of Figures

1. Introduction

1.1 Motivation

Nowadays cameras are widely used to capture a scene or an object as they provide an image that is similar to what we see with our eyes. This is because they record an image for three different channels, red, green, and blue, which correspond to long, middle, and short cones in the human visual system. Although they provide an easy way to capture the appearance of an object with affordable cost, the spectral range of most cameras are restricted to the visible light spectrum. For some cases, however, important information is hidden in the invisible spectrum such as ultraviolet or infrared. That is why the researches for multi- and hyperspectral imaging system were initiated.

A multispectral imaging system has more spectral bands or wider spectral range compared to commercial trichromatic imagers. For instance, an imager that captures a set of ten images from the visible light spectrum is a multispectral imaging system, where another imager, which is able to take eight images from the visible light spectrum and infrared, is also a multispectral imager. The standard for distinguishing hyperspectral imager from multispectral imager is not concrete, but in general we call an imager is a hyperspectral imager if its spectral bands are narrow enough to produce a continuous spectral power distribution of the captured scene.

As it reveals invisible information in a noninvasive manner, applications of hyperspectral imager are spread over broad area. For example, freshness of fruits and health of crops are able to be determined with a hyperspectral image [22, 27]. In the field of medical science, it can be used for diagnosis of several diseases such as retinopathy or certain types of cancer [15, 21]. Furthermore, hyperspectral reflectance measurements not only help mineralogists find the target material, but also used for hyperspectral rendering in computer graphics field.

There are several ways to build up a hyperspectral imaging system. Among them, bandpass filter based method using liquid crystal tunable filters (LCTF) is employed in this proposed imager. Tunable filters have been broadly used to build multi- and hyperspectral imagers as they can provide rapid and vibration-less selection of any wavelength in the visible or near-infrared spectrum. LCTFs are efficient in changing transmittance, have therefore been preferred to build spectral imagers. Although an LCTF can provide a narrow spectral bandwidth such as 7 nm or 10 nm, its spectral coverage is limited to a certain range of visible (VIS), short-near infrared (SNIR), long-near infrared (LNIR) spectrum, etc. Therefore, if a hyperspectral imager using an LCTF is implemented in a straightforward, single optical

path, substituting one LCTF with another in the middle of the capturing process is needed to cover a wider spectrum. In this case, the positions of two LCTFs should be matched as accurate as possible to ensure that the images taken with both LCTFs have the same optical axis. Since it requires extreme carefulness and longer times to take a hyperspectral image, several attempts that split the incident light into two ways using a broad-band polarizing beam splitter have been made.

1.2 Scope

Combining LCTFs with a polarizing beam splitter could be a panacea for the optical axis problem. However, it invokes another problem: owing to the polarization nature in controlling transmittance of LCTFs, it is difficult to employ multiple LCTFs with the beam splitter together.

In this thesis, we propose a simple optical design and implementation of a hyperspectral imaging system. We describe our experience about how to handle multiple polarizing elements to build a hyperspectral imager with two LCTFs of VIS and SNIR to extend the spectral range. We separate the incident light into two directions by positioning a polarizing beam splitter after the light is collimated. This two way design enables us to capture 101 spectral images in a broad spectrum (400 – 1,100 nm) without replacement of LCTFs. Moreover, the images are simultaneously captured with two cameras at the end of the two separated ways, which therefore results in faster acquisition time.

We also deliver explanations for the calibration process of this proposed hyperspectral imager. First, unwanted distortion caused by chromatic aberration and lens distortion is corrected by geometric calibration. Then the relationship between the intensity values of a hyperspectral image and the reference radiance values measured with a spectroradiometer is found in the radiometric calibration process. We evaluate performance of our hyperspectral imager in terms of radiometric accuracy and spatial frequency.

1.3 Contributions

The following contributions are presented in this thesis:

- **An optical design of an hyperspectral imaging system with two LCTFs.** We propose a design of two-way hyperspectral imager which covers a broad spectrum with two LCTFs. Our experience concerning combining multiple polarization equipments is also reported.
- **Radiometric and geometric calibrations for a broad range spectrum.** The calibration process of this proposed hyperspectral imaging system is described in detail. Geometric calibration removes undesirable distortions, whereas radiometric calibration defines the mapping between the captured intensities and the measured radiance values.

Most of these contributions have been presented in the following publication:

- **Haebom Lee** and Min H. Kim, *Building a Two-way Hyperspectral Imaging System with Liquid Crystal Tunable Filters, Proc. Int. Conf. Image and Signal Processing (ICISP)*, June., 2014. (oral presentation)

1.4 Thesis Outline

The remaining part of this thesis is organized as follows. Chapter 2 describes background knowledge that are helpful to understand this thesis. Chapter 3 introduces previous work on hyperspectral imaging system and multi-way optical system. Chapter 4 explains the design of this proposed imaging system and calibration processes. We present the result of the calibration process in a quantitative form in Chapter 5. Summary of this thesis and some limitations of our imager are handled in Chapter 6. Finally, Chapter 7 concludes this thesis. It is followed by Appendices, which illustrates data obtained from the experiment.

2. Background

This chapter presents a brief overview of background knowledge. We first discuss light, in terms of its composition and characteristics. Then we provide explanations for optical instruments that are handled in our experiment. It is then followed by a camera calibration section which describes terms and methods that are commonly used in the camera calibration process. The chapter ends up with preliminaries for multispectral imaging.

2.1 Light

Electromagnetic Spectrum. Light, often referred as visible light, is electromagnetic radiation which can be observed with the human eyes. Although we perceive assorted colors within the visible light spectrum, it comprises only a small portion in the entire electromagnetic spectrum. As illustrated in Figure 2.1, various regions are defined with the wavelength of electromagnetic radiation: gamma rays, X-rays, ultraviolet, infrared, microwave, and radio. Furthermore, it also shows that the color of the light that we perceive is determined by the wavelength of the electromagnetic radiation. If the wavelength

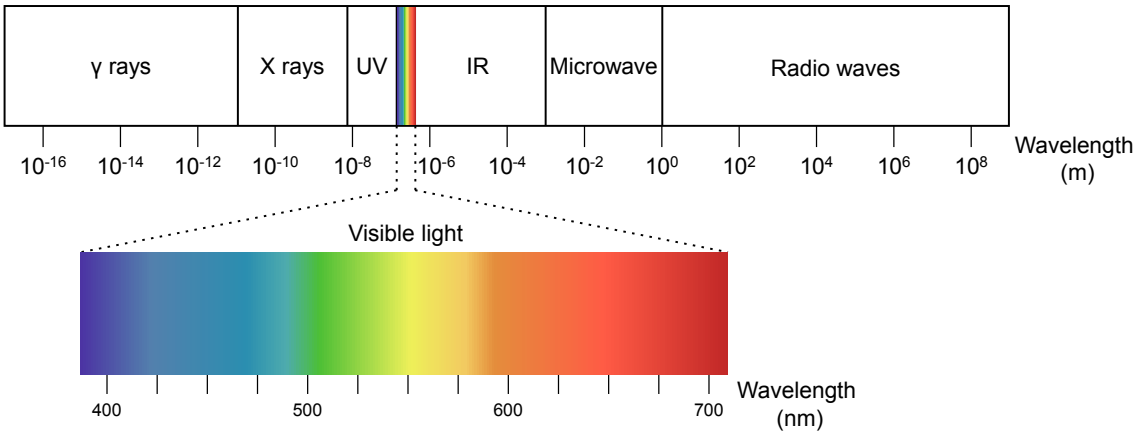

Figure 2.1: *Spectrum of electromagnetic radiation. Each region is defined with the wavelength of electromagnetic radiation. The bottom part shows a magnified image of the visible light spectrum that human can perceive with the eyes.*

of radiation is longer or shorter than that of the visible light spectrum, it becomes invisible to human eyes. However, important information is often hidden in those regions, which therefore encourages us to capture images in the infrared region.

In this thesis, we mainly focus on a spectrum where its wavelength is in a range from 400 nm to

1,100 nm, which therefore contains the visible light spectrum and a small portion of short near infrared spectrum. Note that the short near infrared is a region that next to the right side of the visible light spectrum.

Polarization. Electromagnetic radiation has an intriguing characteristic called polarization, which means that the waves can oscillate in different directions that is perpendicular to the waves' propagation direction. Nonpolarized light, which is commonly observable in our daily lives, is a mixture of those waves that oscillate in different orientations. When it passes through an optical filter, often referred as a polarizer, it becomes a linearly polarized wave. A linearly polarized wave oscillates only in one direction, which is parallel to the direction of the polarizer that it went through. This phenomenon is illustrated in Figure 2.2. It also shows that the linearly polarized wave will be blocked when it propagates to another polarizer that is positioned in perpendicular direction.

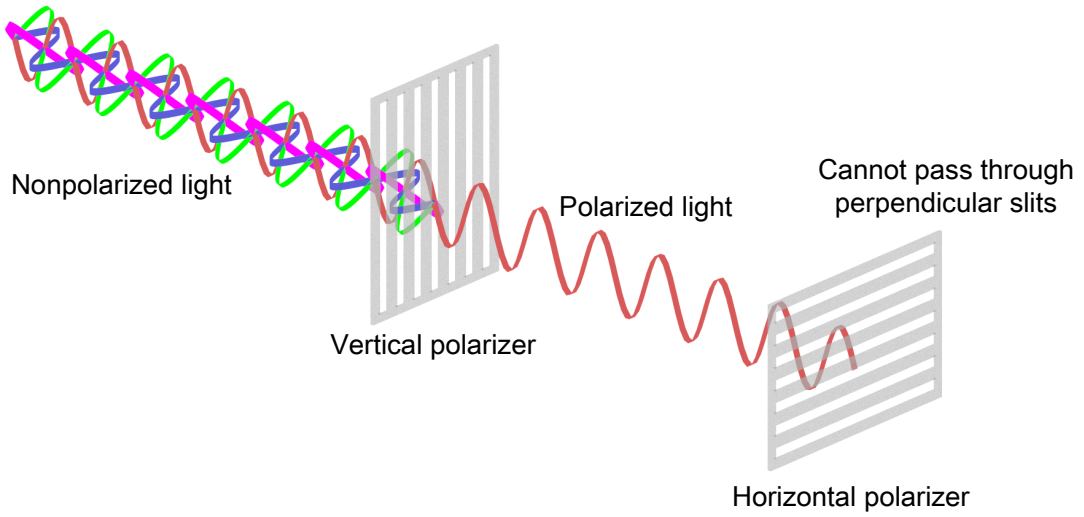

Figure 2.2: *Linear polarization of electromagnetic wave. Once a nonpolarized light passes through a polarizer, it can not go through another polarizer that is perpendicular to the first one.*

There is another type of polarization, called circular polarization. When two linearly polarized light of the same amplitude are combined with 90 degree diffrence in their phases, they constitute a circularly polarized light. Its propagation could be seen as a shape of a spring as illustrated in Figure 2.3. Note that the circularly polarized light has both linearly polarized light denoted by red and blue waves. If it passes through a vertical polarizer, only the vertical component remains unchanged while the horizontal wave is blocked by the polarizer.

The polarization property is inherent in some optical instruments, such as a polarizing beam splitter and a liquid crystal tunable filter. Since those instruments are employed in this proposed imager, we briefly introduce them in the next section.

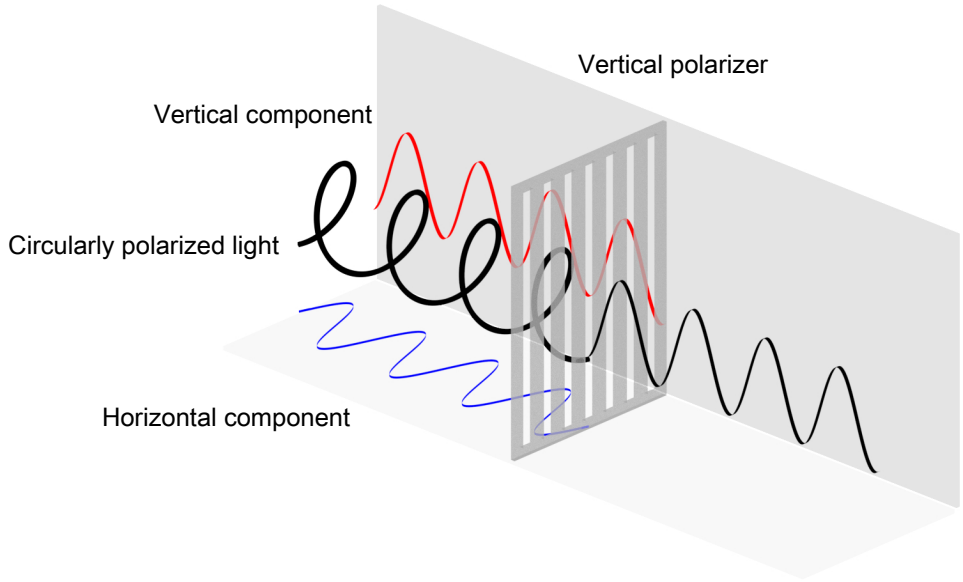

Figure 2.3: *Circular polarization of electromagnetic wave.*

2.2 Optical Instruments

Polarizing beam splitter. A beam splitter is commonly used to divide the incident light into two paths. There are two kinds of shape for beam splitter, cube and plate. Most cube beam splitters are made by attaching two prisms together. The characteristic of a beam splitter is mainly determined by the type of the coating on the internal boundary layer. If a multilayer reflective polarizing film is included in a beam splitter, an incident light is divided into two directions as it passes through a normal beam splitter, but with different polarizations. Figure 2.4 provides a graphical representation of this polarizing beam splitter. The nonpolarized incident light which consists of electric fields with various direction is polarized as two direction, so-called p-polarized and s-polarized [16]. Note that p- and s- for indicating the direction of the polarized light is coming from the word 'parallel' and 'senkrecht (German word for perpendicular)', respectively. The p-polarized light means that the direction of oscillation of the light is parallel to the direction of the slit in the polarizer, whereas the s-polarized light indicates the direction is perpendicular to the slit.

Liquid crystal tunable filter. In order to transmit a specific wavelength range of the incident light, liquid crystal tunable filters are included in this proposed imaging system. An LCTF is widely used in multispectral or hyperspectral imaging systems as it offers fast and accurate selection of a narrow wavelength range via simple USB interface. The detailed internal structure of an LCTF is undisclosed, but it is known that it contains a polarization component made of liquid crystals which controls the transmittance over the supporting spectral range. As there is no single LCTF that can cover the entire spectrum, we use two LCTFs for visible light and near infrared.

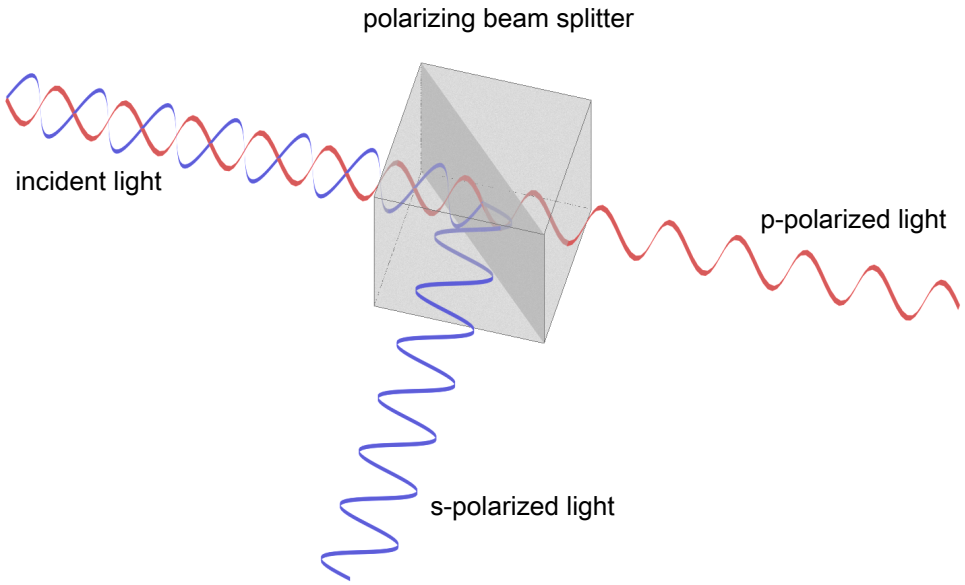

Figure 2.4: *A polarizing beam splitter divides the incident light into two ways. The red wave represents the p-polarized light which oscillates in parallel to the direction of the slit in the beam splitter. If the light oscillates in perpendicular direction like the blue wave, it will be reflected on the internal boundary surface.*

Apochromatic lens. Typical lenses suffer from chromatic aberration, a phenomenon caused by the difference of the wavelength of incoming light. The light with longer wavelength is less refracted than the shorter waves, as illustrated in Figure 2.5 [16]. As our hyperspectral imaging system captures images in

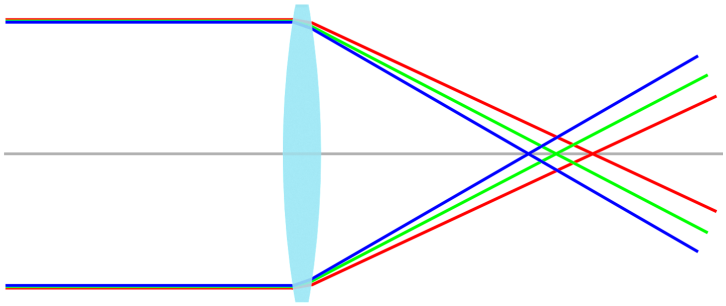

Figure 2.5: *Chromatic aberration of visible light spectrum. Due to the differences on the wavelength, the angles of refraction are not the same. The light with longer wavelength, depicted with red lines, is less refracted compared to the light with shorter wavelength (green and blue lines).*

a broad spectrum (400 – 1100 nm), the size of an object will vary in different images. In order to prevent the problem, an apochromatic lens is employed in this proposed imaging system. The apochromatic lens effectively mitigates chromatic aberration as shown in Figure 2.6. However, when the incident light passes through various optical instruments in the imaging system, the chromatic aberration effect slightly appears again. That is the reason why we perform the camera calibration process.

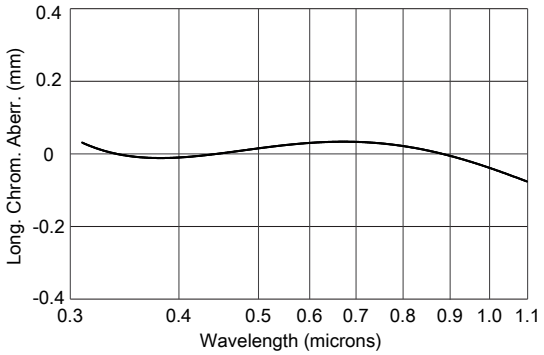

Figure 2.6: *A chromatic aberration plot of an apochromatic lens. Image courtesy of JENOPTIK Optical Systems [18].*

2.3 Camera Calibration

Geometric calibration. Capturing images in different spectral bands causes a target object to be captured in different sizes due to the aforementioned chromatic aberration. Also, images may have unwanted distortion originated from the lenses in the imaging system. Thus we do the geometric calibration process, which enables us to obtain an undistorted hyperspectral image. It can be simply described as finding an affine matrix which transforms a set of coordinates from the distorted image to a set of coordinates from the undistorted, ground truth image. First of all, an image of a checkerboard is captured by the imaging system. Note that we already know the exact position of the corner points of the checkerboard. Then the affine matrix is calculated by solving a simple matrix equation:

$$M_{\text{affine}}\mathbf{x}_{\text{dist}} = \mathbf{x}_{\text{undist}} \,, \tag{2.1}$$

where $\mathbf{x}_{\text{dist}}$ is the set of coordinates of corner points, obtained from the captured image of the checkerboard and $\mathbf{x}_{\text{undist}}$ is the set of known coordinates of the corresponding corner points.

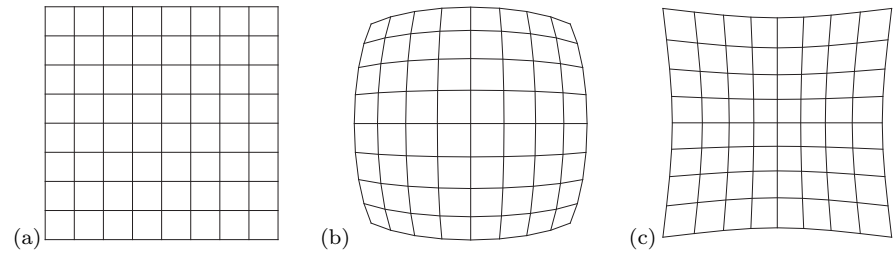

Figure 2.7: *An image of grid (a) will be appeared as (b) or (c) when there is radial lens distortion. Barrel distortion (b) and pincushion distortion (c) are often occurred when using wide-angle lens and tele-photo lens, respectively.*

Figure 2.7 illustrates the effect of lens distortion, which can be approximated as the following

equation [32]:

$$\mathbf{x}_{\text{undist}} = \mathbf{x}_{\text{dist}}(1 + k_1 r^2 + k_2 r^4)\,, \tag{2.2}$$

where k_1 and k_2 are the lens distortion coefficients, and r is the distance from the center point. Similar to the correction for chromatic aberration, we can remove the lens distortion effect by estimating the lens distortion coefficients from the corresponding coordinates of corner points. Note that this process should be done after the calibration of chromatic aberration.

Radiometric calibration. Geometric calibration is the process that finding a relationship between the distorted image and the reference image. Likewise, in the radiometric calibration process, the connection of the measured intensities and the reference radiance values is determined. The radiance values of 25 training colors are measured with a spectroradiometer to be used as the reference. As this proposed imaging system is able to deliver the intensity of the target in different spectral bands, the following linear transformation holds for each spectral band λ:

$$I_\lambda = T_\lambda L_\lambda \ , \tag{2.3}$$

where I_λ is the image intensity value, T_λ is the transformation, and L_λ is the reference radiance value. Note that the T_λ hides the underlying optical characteristics such as quantum efficiency or transmittance efficiency. Detailed explanation for Equation (2.3) will be delivered in Section 4.3.

3. Related Work

Hyperspectral imaging systems can be categorized into either bandpass- or dispersion-based systems. This chapter overviews relevant previous work.

3.1 Dispersion-Based Imaging Spectroscopy

3.1.1 Pushbroom-Based Systems

Pushbroom-based imaging systems measure spectrum by moving the sensor along the dispersion direction. In general, the spectral resolution of such systems is determined by its optical design, i.e., the number of pixel within the spectral range measured. These systems are commonly used in air- and space-borne scanners due to high spectral resolution. Besides the benefit for spectral resolution, general pushbroom systems suffer from artifacts that can exacerbate the identification of feature's composition as well as the classification of pixels. Mouroulis et al. [26] introduced an optimized design for the pushbroom imaging spectroscopy. Prior pushbroom systems suffered from artifacts that can exacerbate the identification of feature's composition as well as the classification of pixels. They therefore proposed a frequency-based optimization method that allows to reconstruct spatially uniform spectral information from the pushbroom systems. Keystone error is another obstacle in pushbroom-based systems. Several solutions are proposed to mitigated the errors, but often results in reduced amount of light and decreased spatial resolution. Recently, Hoye et al. [17] presented a pushbroom camera system by physically attaching a set of light mixing chambers to the slit. Their pushbroom optics design enabled them to reduce typical artifacts in hyperspectral cameras, e.g., keystone and smile as well as achieve four times more light compared to ordinary pushbroom-based imager .

3.1.2 Snapshot-Based Systems

Dispersion-based imaging systems measure a spectrum dispersed by either a diffraction grating or a prism [34]. Du et al. [9] devised a prism-based multispectral video acquisition system. The occlusion mask employed in their system worked as a sampling tool and each sampled light is dispersed by a prism. The spectral coverage of this system can be adjusted by changing the focal length of the camera. This proposed method also includes calibration processes in both radiometric and geometric point of view. Although this system provides relatively narrow bandwidth (up to 2 nm), the spatial resolution and the frame-per-second value are sacrificed in proportion. Habel et al. [13] proposed an advanced imager in terms of

spectral resolution. The imager is formed with relatively cheap apparatuses while providing up to 4.89 nm spectral resolution (54 spectral bands); its spatial resolution is limited to 120×120 pixels. It can be also used as a column based spectral imager where the spectral resolution can be increased up to 0.8 nm. Their contributions include a mathematical approach for reconstructing spectral information from a conventional Bayer pattern image. The computed tomography imaging spectrometry allows to capture high spectral resolution, but its image resolution and post-processing time are limited. Kim et al. [19] introduced a 3D imaging spectroscopy (3DIS) system, yielding complete 3D models with hyperspectral reflectance from 369 nm to 1,003 nm at 12 nm spectral resolution. Integrating a coded aperture and a prism-based hyperspectral imaging system, they achieved higher spatial and spectral resolution. Such a precise measurement enabled them to obtain a physically meaningful 3D hyperspectral patterns of a target. As their method requires optimization process to derive underlying spectral information from the dispersed image, the post-processing step needs reasonable time. In this thesis, we compare the performance of our hyperspectral imaging system with 3DIS system.

3.2 Bandpass Filter-Based Imaging Spectroscopy

3.2.1 Filter-Based Systems

General bandpass filter-based imaging systems include a set of narrow bandpass filters on a wheel. These filters are used to discriminate the incident light into narrow bands. The spectral bandwidth of such systems is limited to approximately 15 nm by the bandwidth property of the filters. Rapantzikos et al. [31] implemented a bandpass-based hyperspectral imager that consists of an imaging detector and a set of narrow bandpass filters. This imager extracts 34 spectral bands in a range of $360 - 1{,}150$ nm with spatial resolution 1280×960. They utilized this imager for non-destructive examination of cultural heritages. Brauers et al. [4] introduced a mathematical model for eliminating geometric distortions in multispectral images. They parameterized and estimated the optical distortion coefficients in the affine space by using the RANSAC method [11]. Their multispectral system includes a set of seven bandpass filters, attached on a wheel, and yields seven multispectral images in the visible light spectrum with 40 nm bandwidth. Mansouri et al. [24] integrated a multispectral camera into a 3D scanning system. The camera includes a set of seven bandpass filters and is leveled same as an LCD projector, which operates as a vertical line illumination that spans the object. Although the bandwidth of the system is limited to the visible light spectrum due to the bandwidth of the filters, their system is compelling against high-cost off-the-shelf products. They also introduced the applications of the hyperspectral imaging system, for example, a virtual museum.

3.2.2 Tunable Filter-Based Systems

A tunable filter can be electronically controlled to change its spectral transmittance by applying voltage [12]. LCTFs are popularly used as they can provide the spectral resolution of the order of several nanometers with a narrow bandwidth such as ∼7 nm. Different from the pushbroom systems, the tunable filter-based systems require less computation and result in fewer artifacts than dispersion-based imaging. Attas et al. [3] focused on a phenomenon that the difference of various pigments is prominent in near infrared spectrum. Therefore, they proposed a hyperspectral imaging system which adapts an LCTF for near infrared spectroscopic imaging, where the bandwidth of the imager was 10 nm. This proposed hyperspectral imager is then utilized for specification of diverse pigments in cultural heritages. Hardeberg et al. [14] measured the spectral reflectance of the imaged surface using an LCTF and a monochrome camera, yielding a 17-channel hyperspectral image in visible spectrum. In order to obtain device-independent color measurement, they tested two methods: a simple linear regression by recovering the CIEXYZ color coordinates and establishing a spectral model of the imaging system. In this paper, we propose a hyperspectral imaging system that obtains 101 spectral bands in a spectral range of 400 – 1,100 nm with two LCTFs of ∼7 nm bandwidth. Furthermore, the imager operates twice as fast as the previous system with help of a two-way imaging structure.

3.3 Multi-Way Imaging Systems

Beam-splitting design has been commonly used in advanced imaging systems. In general, if we split a beam into n beams, the radiative power of the beam on each sensor reduces to $1/n$ of the entering power. Wolff [36] presented a polarization camera with a beam splitter and two cameras. This seminal system can distinguish specular and diffuse reflection from metal material. Our system in particular inherits this fundamental design of two-way optics. Aggrawal and Ahuja proposed a high-dynamic-range (HDR) imaging system with multiple imaging sensors and a beam-splitting prism [1]. In this system, the distance between the sensor and the prism determines the exposure variation, which allows to build HDR images with globally varying exposures. McGuire et al. [25] proposed the design of monocular multiview optical systems with recursive optical splitting trees. They provided an HDR imaging application with the advanced splitting mechanism. Moreover, by employing multiple dichroic mirros in their splitting trees, the system could operate as a bandpass filter-based multispectral imaging system. Tocci et al. [33] introduced advanced HDR imaging system based on the beam-splitting mechanism with efficient use of the available light. They precisely determined angles of beam splitters, so that the amount of light enters into each camera differs without use of absorptive filters. This method therefore results in increased light efficiency, which enabled their HDR merging algorithm geared toward high-definition HDR videos.

4. Two-way Hyperspectral Imaging System

4.1 System Design

The fundamental optical path of our system inherits the traditional multi-way systems [36]. However, we design our optics to broaden the spectral coverage of our system by carefully choosing optical components. The arrangement of the components and the light path of our system are designed and verified with a simulation by Zemax [37] before we build it. Incoming light enters through the first component of our system, an apochromatic objective lens (CoastalOpt UV-VIS-IR 60 mm). This lens offers focused images regardless of incident spectrum within our target range (400 – 1,100 nm). A FS Cooke-triplet lens with 50 mm focal length is used to collimate the focused light to make it propagate in parallel along the optical axis through the rest of our system. The parallelized beams hit the broad-band beam splitter (Spectral Optics), which transfers spectrum in between visible light and infrared light (450 – 1,500 nm). We locate two Varispec LCTFs: the visible LCTF (VIS-07-20) covers spectrum range from 400 nm to 720 nm, and the infrared LCTF (SNIR-07-20) covers 650 – 1,100 nm, respectively along the direction of the split two-way light paths. See Figure 4.1. Both LCTFs work as simple yet effective electronic narrow bandpass filter. At the end of the light path, the beams within the specified spectral range enter into a focusing lens. Finally, the intensity of the focused image is recorded via a positive triplet lens with 50 mm focal length by a monochrome camera (PointGrey FL3) on each light path. See Figure 4.2 for our system and its optical design.

4.2 Polarized Light Path

Since we are set to build a hyperspectral camera, we chose a hyperspectral beamsplitter based on polarization, rather than coating. The beamsplitter polarizes the incident light as well as splits it into two ways. The light which consists of electric fields with various direction, is polarized as two direction, so-called p-polarized and s-polarized [16]. The p-polarized light means that the direction of oscillation of the light is parallel to the direction of the slit in the polarizer, whereas the s-polarized light indicates the direction is perpendicular to the slit. As the direction of the polarized light becomes different after the incident light is divided, we have to set the direction of the LCTFs perpendicular to each other as shown in Figure 4.2(a). Otherwise, no image would be gained as no light passes through two polarizers. Note that we capture images with 50% of the incident light on each camera at the end of the light path via the

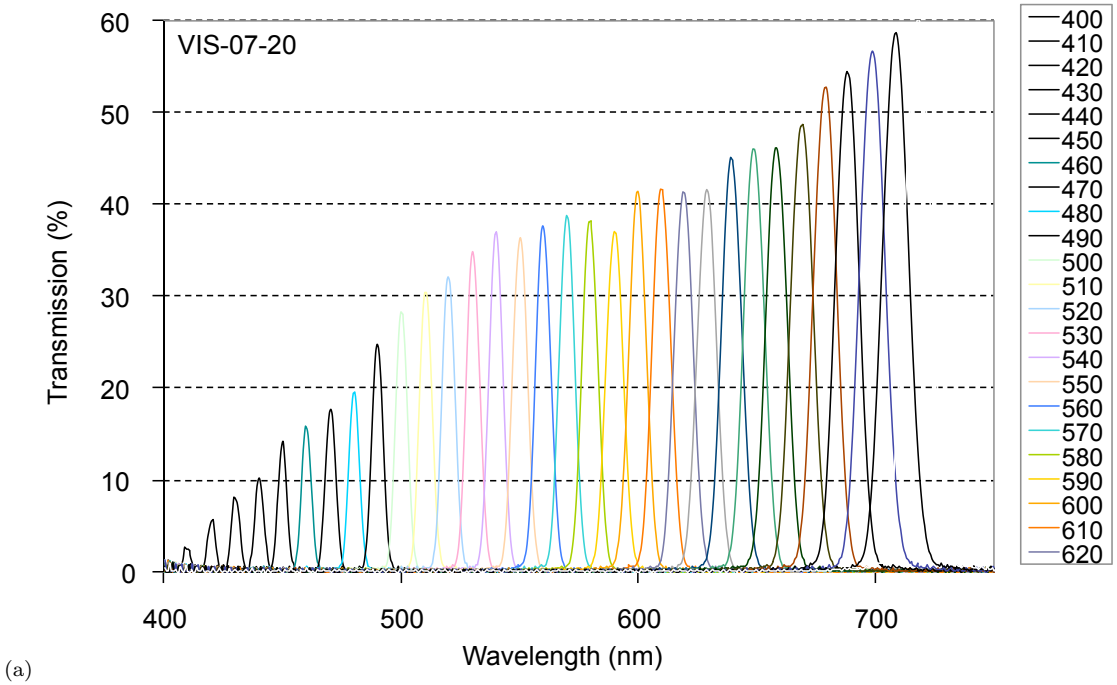

(a)

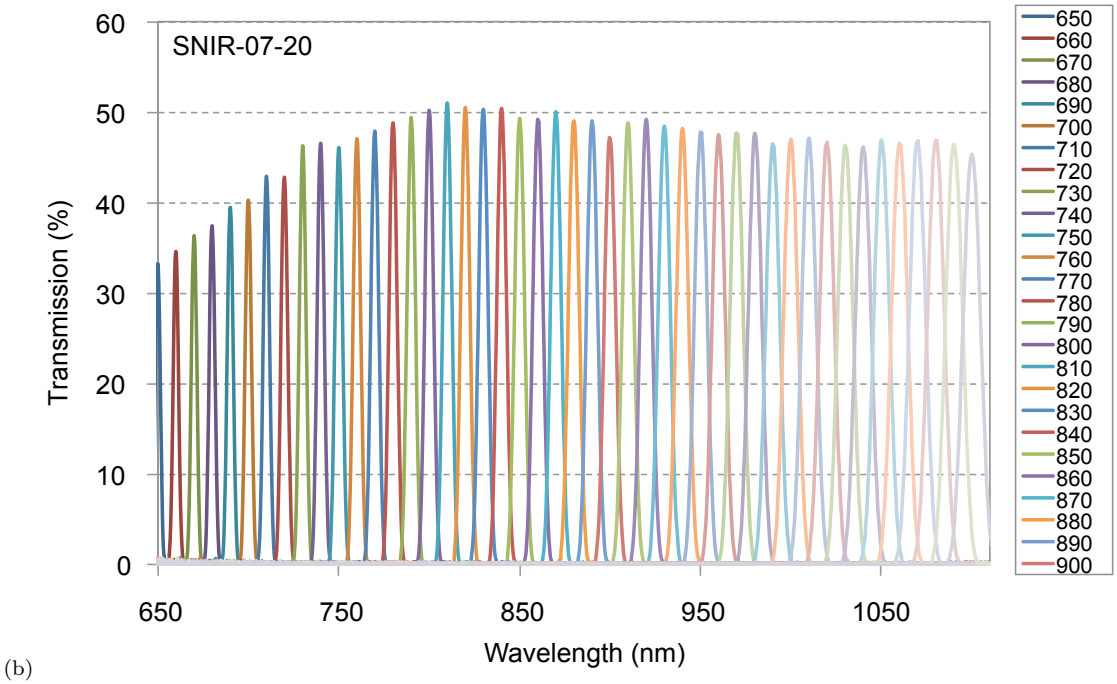

(b)

Figure 4.1: *Spectral transmittance of the two LCTFs of CRi VariSpec series, employed in our imaging system. (a) VIS-07-20 visible transmittance. (b) SNIR-07-20 short near-infrared transmittance. Images courtesy of PerkinElmer Inc. [30].*

(a)

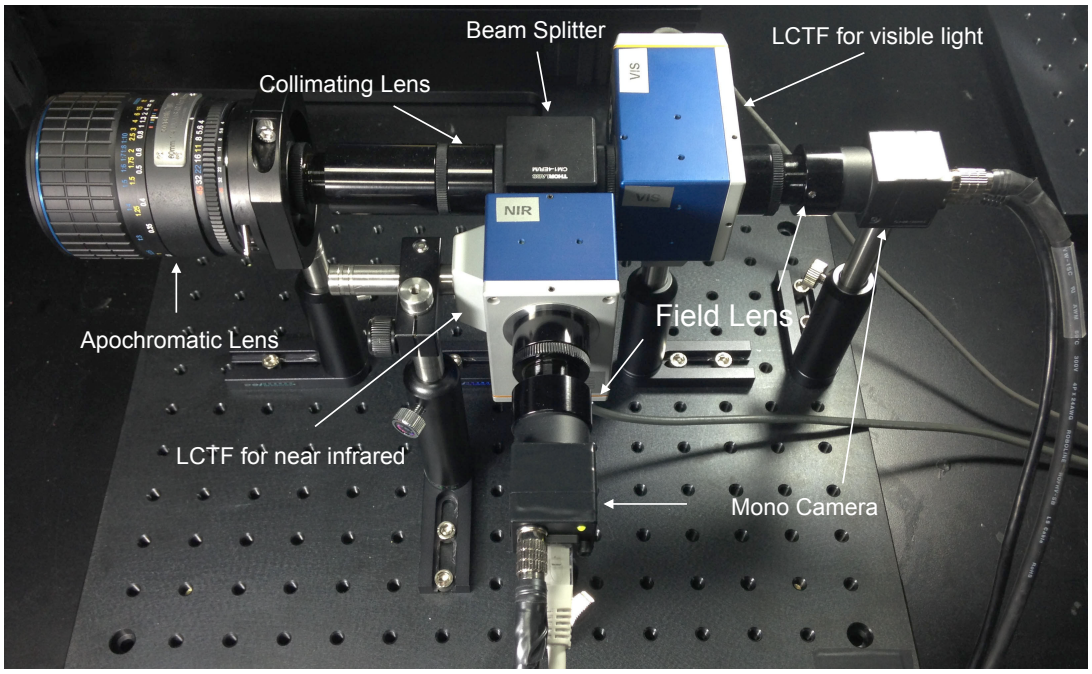

(b)

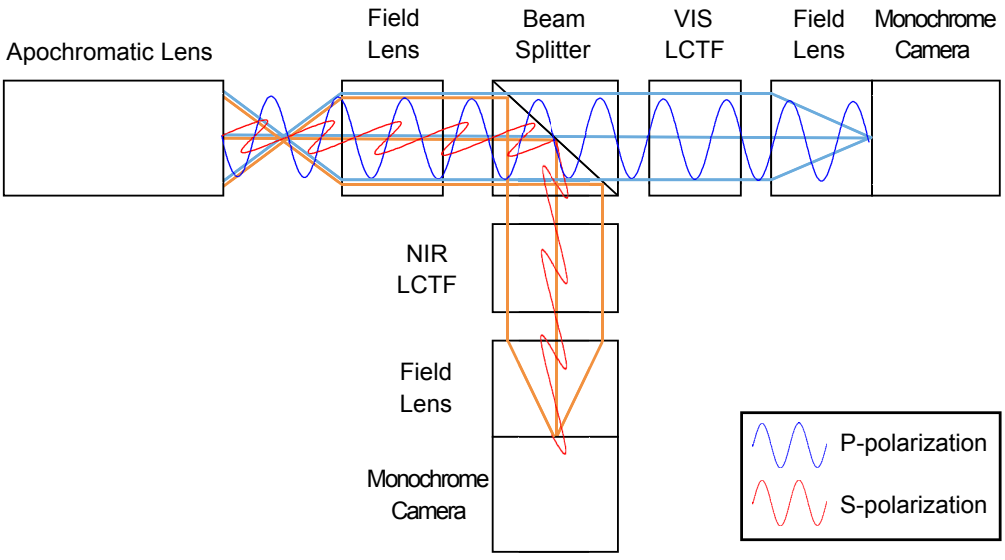

Figure 4.2: *(a) Our hyperspectral imaging system and (b) its polarized light path*

LCTF, respectively due to the polarization-based design. Furthermore, as illustrated in Figure 4.2(a), when the beamsplitter reflects 50% of its incident light it causes horizontal reflection on an image captured by the monochromatic camera at the reflected light path. This phenomenon is easily observable by tracking the light starts from the end of the apochromatic lens. A light emitted from the left side of the apochromatic lens enters into the camera from the right side if it is not reflected. The reflected light however arrives at the camera along the path that starts from the left side of the camera. Another virtue of our two-way design is that we can obtain images from both cameras simultaneously, making our system take only 160 seconds for capturing an 101-channel hyperspectral image in total (shutter speed per shot: 1.5 seconds).

4.3 System Calibration

We then calibrated the radiometric and geometric properties of our hyperspectral imaging system for physically-meaningful measurements.

Radiometric Calibration. The response function of our imaging system can be described as a linear product of the quantum efficiency at each wavelength Q_λ of the monochromatic sensor, the transmittance efficiency T_λ through the optical path, and the transmittance functions of two LCTFs (i.e., $F_{\mathrm{VIS},\lambda}$ and $F_{\mathrm{SNIR},\lambda}$). We define the camera response function $f_{\mathrm{BAND},\lambda}$ of each filter band (of VIS and SNIR) as follows:

$$f_{\mathrm{BAND},\lambda} = Q_\lambda T_\lambda F_{\mathrm{BAND},\lambda} L_\lambda \ , \tag{4.1}$$

where L_λ is the radiance that enters to the camera system. In order to convert the raw signal levels to the incident radiance, we determine a linear transformation C_λ that describes $(Q_\lambda T_\lambda F_{\mathrm{BAND},\lambda})^{-1}$. We measured a set of 25 training colors, including an X-rite ColorChecker and a Spectralon (calibrated to 99%) under two halogen lights. We find a linear mapping function C_λ of the raw signals that correspond to the incident radiance. The multiplication of the $f_{\mathrm{BAND},\lambda}$ and C_λ yields the physically-meaningful radiance L_λ. See Figure 5.4(a) for the training colors.

Geometric Calibration. Although we employ an apochromatic objective lens and a set of field lenses made of Fused Silica with concern of the spectral transmittance, an incident ray refracts slightly differently according to its wavelength. This refraction effect results in forming images in different sizes per wavelength. In order to calibrate this optical geometric mismatch, we first capture a standard checker board, and for each wavelength we manually collect the image coordinates of corners. We determine an affine transform per each spectral channel A_λ to calibrate geometric distortion per wavelength. We then

apply each affine transform for warping each spectral channel L_λ to the reference image (at 554 nm), yielding the hyperspectral radiance L'_λ along the wavelength axis as follows:

$$L'_\lambda = A_\lambda L_\lambda \ . \tag{4.2}$$

Note that the spectral channel of reference image is chosen as 554 nm because it corresponds to green color, which the human visual system has maximum resolution.

From the coordinates of corner points of checker board, we can also determine the lens distortion coefficients. Lens distortion, mainly appears as the barrel distortion, affects the entire image as described in Section 2.3. Under the assumption that the tangential distortion is not severe and the radial distortion primarily depends on the first two terms, we can simplify the equation in [32] as follows:

$$\begin{aligned} x_{\text{undist}} &= x_{\text{dist}}(1 + k_1 r^2 + k_2 r^4), \\ y_{\text{undist}} &= y_{\text{dist}}(1 + k_1 r^2 + k_2 r^4), \end{aligned} \tag{4.3}$$

where r is the distance from the image center to a point (x, y). It is possible to evaluate coefficients k_1 and k_2 from the coordinates of corresponding points in a distorted image and the standard undistorted image using OpenCV [29] calibrateCamera API. The coefficients are then used to undistort the input image.

Color Calibration. Once we capture hyperspectral radiance, we store it as a 2D float image in multi-layers in the OpenEXR format [23]. In order to present visible spectral information as a color image, we project the spectral layers L'_λ to the tristimulus values using the CIE color matching functions M_{XYZ} of 2-degree observation [8]. We then transform the tristimulus values in CIEXYZ to the sRGB color values C_{RGB} using the standard sRGB transform M_{sRGB} [28] and then apply either the gray-world white balancing algorithm [5] or the manual white balancing by manually determining the reference white in the scene:

$$C_{\text{RGB}} = M_{\text{sRGB}} M_{\text{XYZ}} L'_\lambda \ . \tag{4.4}$$

Finally, these color calibrated images C_{RGB} are displayed via the gamma correction (γ=2.2). See Figure 5.4 for the color images that we captured with our imager.

4.4 Experimental Procedure

This section explains detailed procedure of our experiment. We first perform the calibrations for our imaging system to find out the linear transformations C_λ in radiometric calibration and affine trans-

formations A_λ in geometric calibration. Then we evaluate the radiometric accuracy of our imager by calculating coefficient of variation (CV) between the measured values and the reference values. Spatial frequency response is also measured to estimate the spatial resolution of our system. Finally, we examine the result of color calibration to check its accuracy in terms of perceptual difference compared to the reference value.

Performing Camera Calibration. We take hyperspectral images of a checker board and two sets of color patches for training and test. From the checker board image, we figure out per channel affine transformation matrix with respect to the reference image (at 554 nm). Furthermore, the imaging system's lens distortion coefficients are drawn from the comparison between the coordinates of corner points in the reference image and the undistorted, ground truth image. We draw plots of obtained intensity values versus measured radiance values for each spectral channel. Using a linear regression method, we are able to find the slope of a plotted line, which becomes the ratio between the intensity value and the radiance value. We apply the affine transformation and the linear transformation to input hyperspectral image to attain the geometrically and radiometrically calibrated hyperspectral image.

Radiometric Accuracy Evaluation. We compare the radiometric accuracy of our hyperspectral imager with reference measurements (measured by a calibrated hyperspectral spectroradiometer, OceanOptics USB 2000, revised for wider spectral sensitivity). Since we built a hyperspectral camera, which has twice-wider dynamic range than the human visual system, the general color difference evaluation such as CIE ΔE_{00} is not a proper evaluation standard for our system. Instead, the coefficient of variation (CV) between our hyperspectral imager and the radiometric measurements is calculated by dividing the root-mean-squared error (RMSE) by mean. We present the evaluation results for both a training set consists of 25 colors and a test set consists of 8 colors in the next chapter.

Measuring Spatial Frequency Response. In order to evaluate the spatial resolution of our imaging system, we capture a hyperspectral image of ISO 12233, a standard frequency target [6]. We chose the target since the slanted-edge analysis effectively alleviates aliasing resulting from the Bayer pattern on a camera sensor and does not heavily rely on the printing quality of the target. The procedure for measuring SFR from a slanted-edge has been well established [6, 7] and widely used for imaging system inspection [35, 38]. Figure 4.3 illustrates how an image of slanted-edge is transformed to a metric, SFR. First, we crop the slanted-edge regions manually. The next step is computing first-order derivatives for each line and locating the center of the edge. Then we can obtain the super-resolution edge spread function by applying linear regression on the centers of each line and aggregating image data along the direction of the estimated edge. Finally SFR is evaluated from the Fourier transformed first derivatives of the super-resolution edge. Note that it is possible to refer the SFR as an estimated modulation transfer function (MTF) after we normalize SFR with the response at frequency zero.

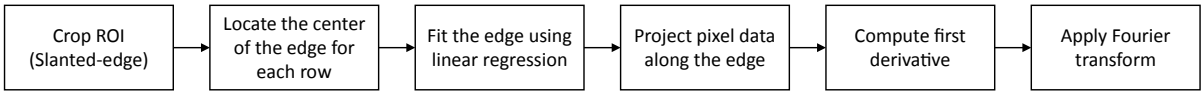

Figure 4.3: *Procedures for measuring spatial frequency response from an image of slanted edge.*

Evaluating Color Calibration Accuracy. We can also evaluate the perceptual difference between the color calibration result and the reference measurement. See Figure 4.4 for the entire process. First, the CIEXYZ values obtained from the hyperspectral image are now converted to points on the CIE 1976 Uniform Chromaticity Scales (UCS) diagram. See Figure 4.5. Using the UCS diagram for calculating difference between the calibrated color and the ground truth color is meaningful as the Euclidean distance on the diagram depicts the perceptual distance of colors. The transformation from the CIEXYZ coordinates is as simple as follows [10]:

$$\begin{aligned} u' &= 4X/(X + 15Y + 3Z), \\ v' &= 9Y/(X + 15Y + 3Z). \end{aligned} \tag{4.5}$$

We obtain the reference u', v' coordinates from the CIEXYZ values measured with a spectroradiometer. Finally, the mean and standard deviation of $\Delta u'v'$ will be calculated from the Euclidean distance between the corresponding points.

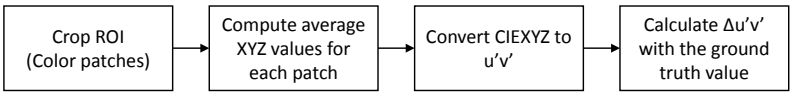

Figure 4.4: *Procedures for measuring perceptual difference of color calibration result.*

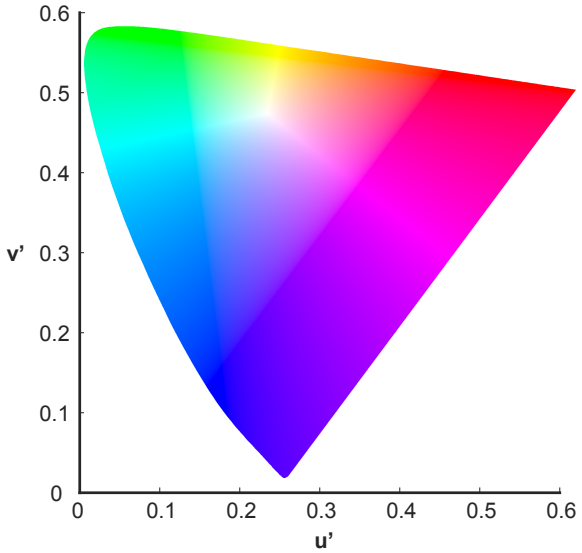

Figure 4.5: *CIE 1976 UCS Diagram. The Euclidean distance of two colors on this diagram reflects the perceptual difference between them.*

5. Results

In this section, we provide quantitative evaluations for our imaging system as well as the results of this proposed calibration methods. Hyperspectral images of a checker board and two sets of color patches are captured with our hyperspectral imager. We first performed geometric calibration using the hyperspectral image of a checker board. In this procedure, the effects of chromatic aberration and lens distortion are calibrated. After then, the hyperspectral image of training color patches are used to calibrate the system. The result of this radiometric calibration is evaluated with the hyperspectral image of test color patches.

5.1 Geometric Calibration

The effect of chromatic aberration is illustrated in Figure 5.1. The differerences of two images taken from 498 nm and 1002 nm respectively are conspicuous, and the peak signal to noise ratio (PSNR) is calculated out as 36.2822. After the geometric calibration that we described in the previous chapter, the images are aligned with respect to the reference image (at 554 nm). Figure 5.2 shows that differences of two images are reduced where the PSNR is now increased to 38.5057. However, the images still suffer from lens distortion. We calculated the lens distortion coefficients from the coordinates of corner points in reference image (at 554 nm) and the corresponding coordinates of corner points in the ground truth image. The lens distortion coefficients k_1 and k_2 in Equation (4.3) are calculated as 239.3318 and 1.1357, respectively. In Figure 5.3, the lines of the checkerboard in the distorted image becomes more parallel in the undistorted image. The PSNR of two images is 29.4586.

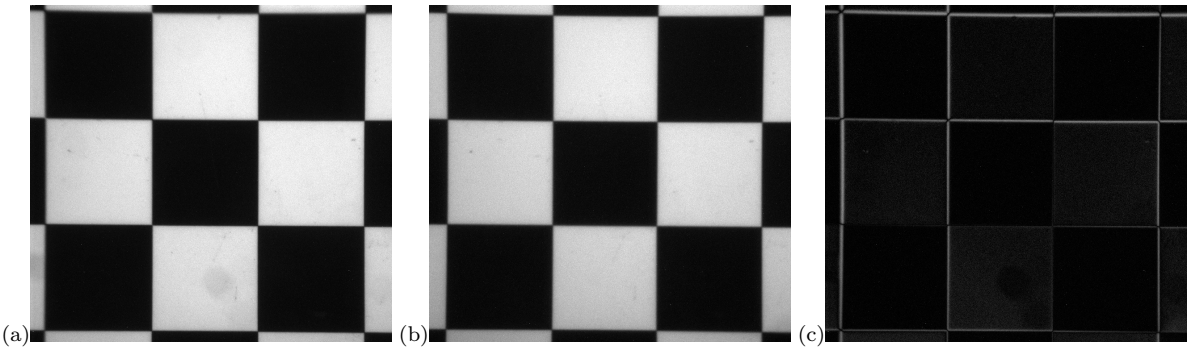

Figure 5.1: *The hyperspectral image of a checkerboard shows significant differences due to the chromatic aberration. The left image (a) is an image of 498 nm and the center image (b) is an image of 1002 nm. Differences of two images are definite in the right image (c), where the peak signal to noise ratio (PSNR) between the images is 36.2822. Note that the brightness of the images are modified to provide a better view.*

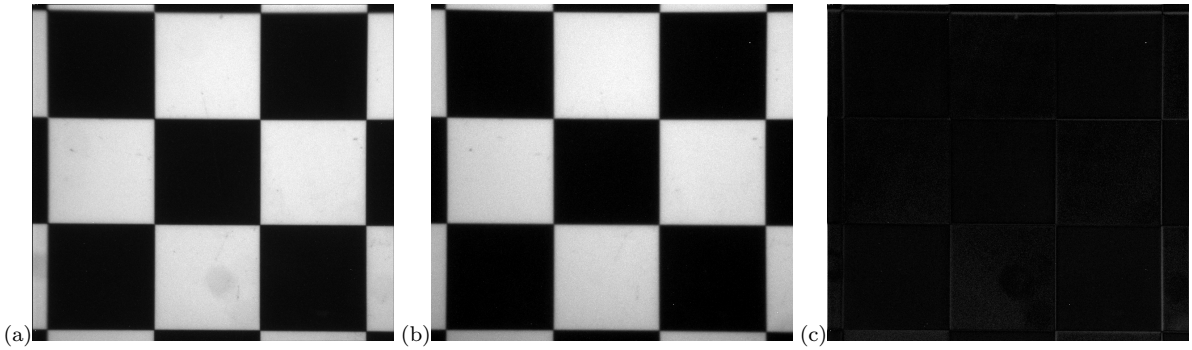

Figure 5.2: *The images (a) and (b) shows the calibrated results for 498 nm and 1002 nm, respectively. As illustrated in (c), the differences of two images are reduced, and the PSNR value is increased to 38.5057. Note that the brightness of the images are modified to provide a better view.*

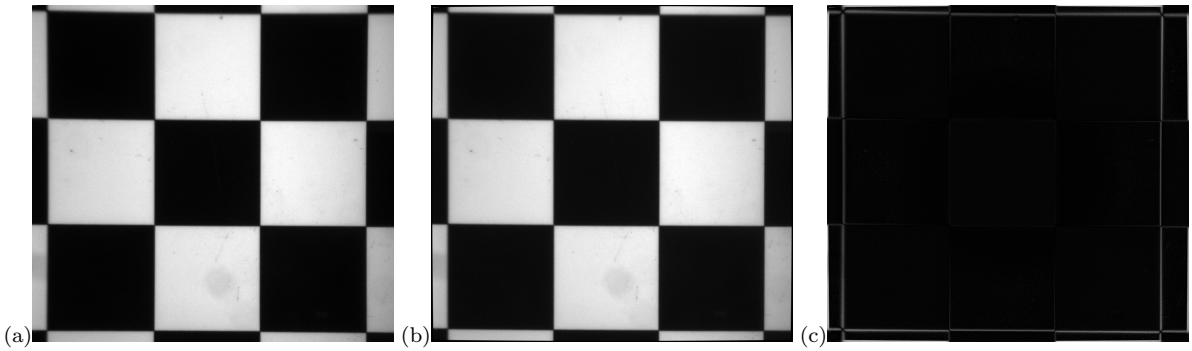

Figure 5.3: *The differences between the distorted image (a) and the undistorted image (b) are presented in (c), where the PSNR is 29.4586. Note that the brightness of the images are modified to provide a better view.*

5.2 Radiometric Accuracy

The result of radiometric calibration is illustrated in Figure 5.4. At the top, there are sRGB images of training and test color patches, respectively. Radiance plots for red, green, blue color patches in training and test set are also shown in Figure 5.4. As mentioned before, the accuracy of radiometric calibration is evaluated with CV values. The CV values on the 25 training colors (24 color patches and spectralone) and on new eight test colors are 13% and 9%, respectively. Figure 5.5 compares the radiometric accuracy of our system with a snapshot-based hyperspectral imager (3DIS) [19], a bandpass-based hyperspectral camera (QSI 583WS) [20] and a characterized RGB camera (Nikon D100), measured on the standard ColorChecker. Our system consistently outperforms other imaging systems in terms of radiometric accuracy. In addition, the spectral resolution of our system (101 channels) is about twice as high as the 3DIS system [19] (53 channels).

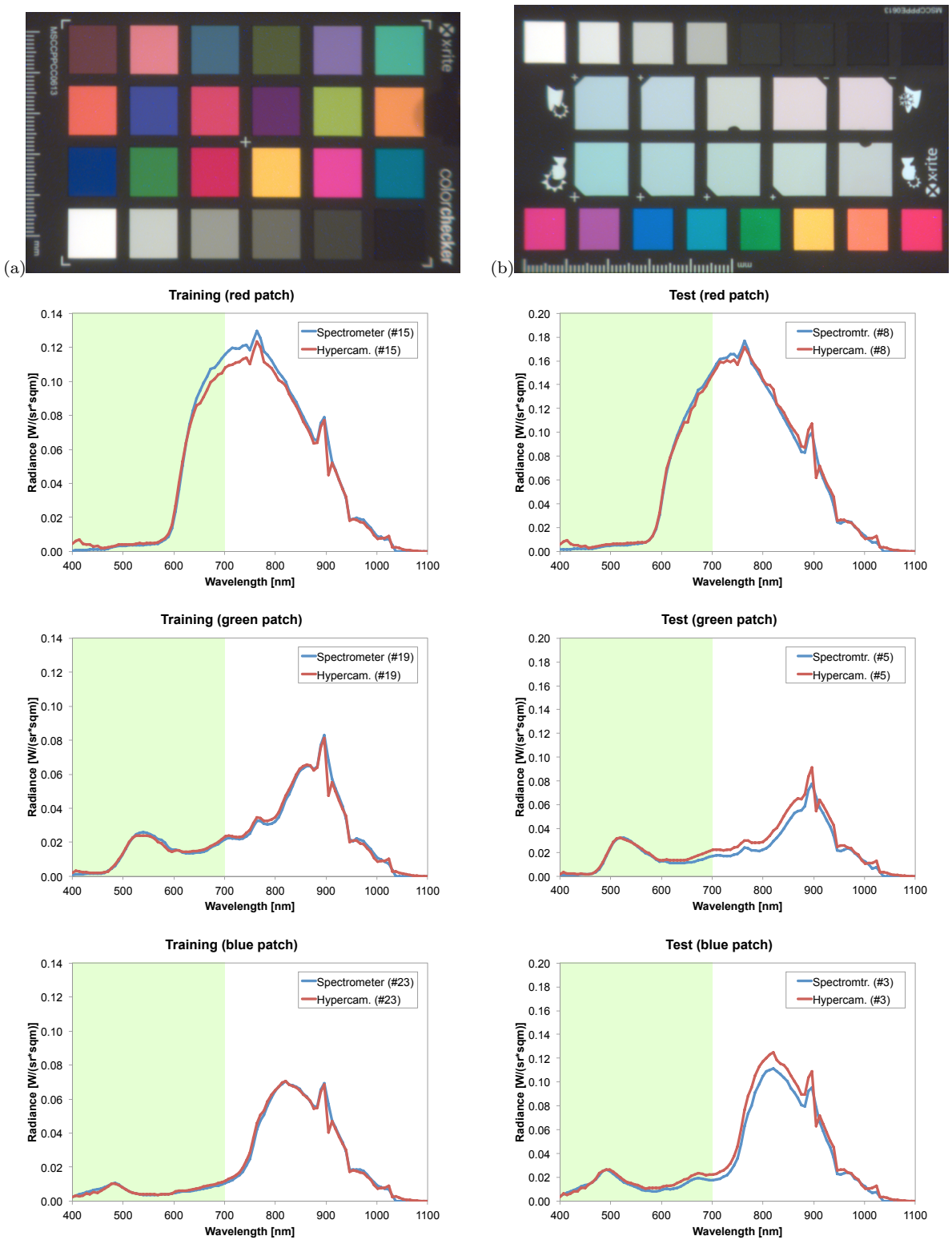

Figure 5.4: *The left column (a) presents the training color patches, captured by our hyperspectral imager, followed by the radiance plots of the red, green and blue patches. The red line in the plots indicates the spectral measurement by our imager; the blue line indicates the measurement by the spectroradiometer; The green spectral region on these plots indicate the human visible spectrum. The right column (b) shows the test color patches, followed by the radiance plots of the test color patches (red, green and blue from the right).*

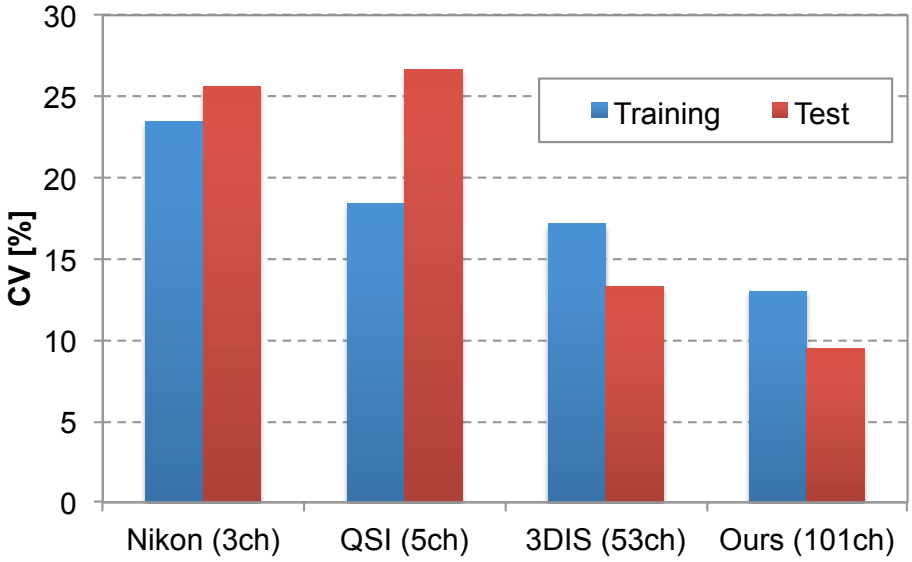

Figure 5.5: *Comparison of coefficients of variation (CV) of four imaging systems: a characterized RGB camera (Nikon D100), a bandpass-based hyperspectral imager (QSI, 5 ch. [20]), a snapshot-based hyperspectral imager (3DIS, 53 ch. [19]), and our system (101 ch.).*

5.3 Spatial Frequency

As mentioned in Section 4.4, we evaluate the performance of the spatial frequency of our system by measuring the spatial frequency response (SFR) with a standard frequency target, ISO 12233. Figure 5.6 compares the spatial resolution of our hyperspectral imager with a state-of-the-art snapshot-based hyperspectral imager, 3DIS [19] in terms of the horizontal and vertical SFRs. Figure 5.6(a) shows the spatial resolution in the visible spectrum, where Figure 5.6(b) presents the resolution in the infrared spectrum. The spatial resolving power of our system is lower than that of the 3DIS system [19] due to the optical design of the collimating lenses and the position of the LCTFs in the optical path. We discuss the reasons and possible solutions for low SFRs in detail in the next chapter. We also calculated the MTF50 values for both directions and for both LCTFs. The MTF50 value is defined as the frequency where the response is equal to 0.5. As the MTF50 is a single value that can represent the sharpness of an imager, it is widely used as a metric for spatial resolution. The calculated horizontal and vertical MTF50 values of our system are 0.080645, 0.074627 for the visible light spectrum and 0.0625, 0.080645 for the near infrared spectrum, respectively. Although the MTF50 values of our system are not as high as the values of 3DIS, note that the spatial resolutions of both ways in our system are so close that any specific resolution of both bands is not biased in a certain axis.

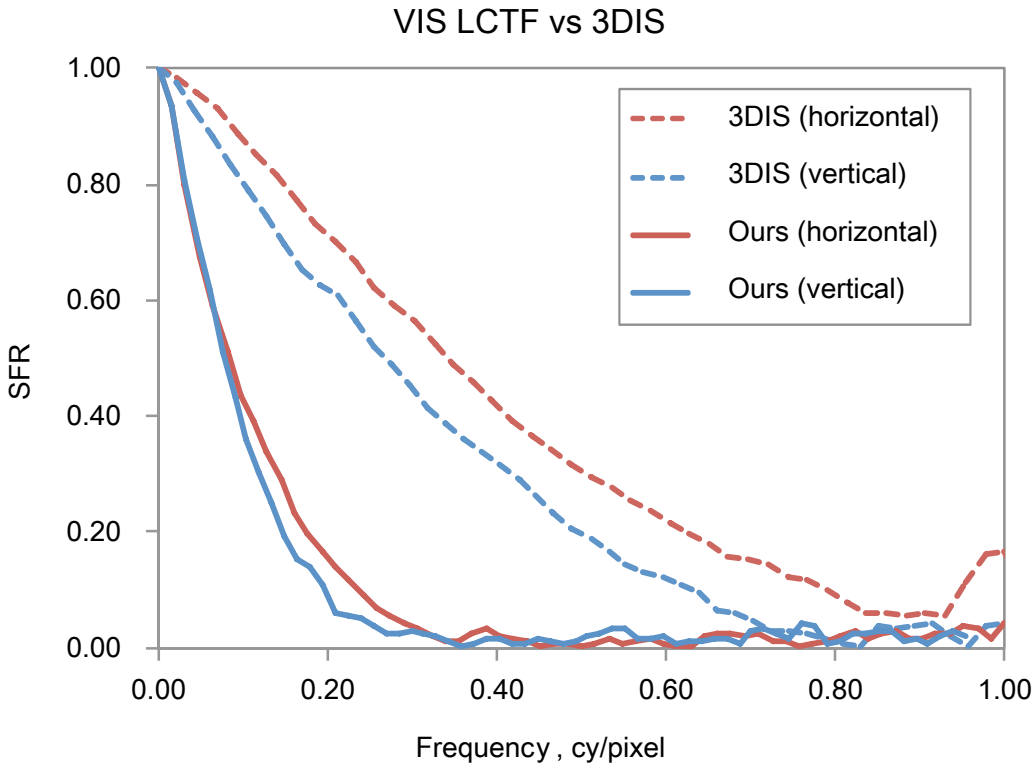

(a)

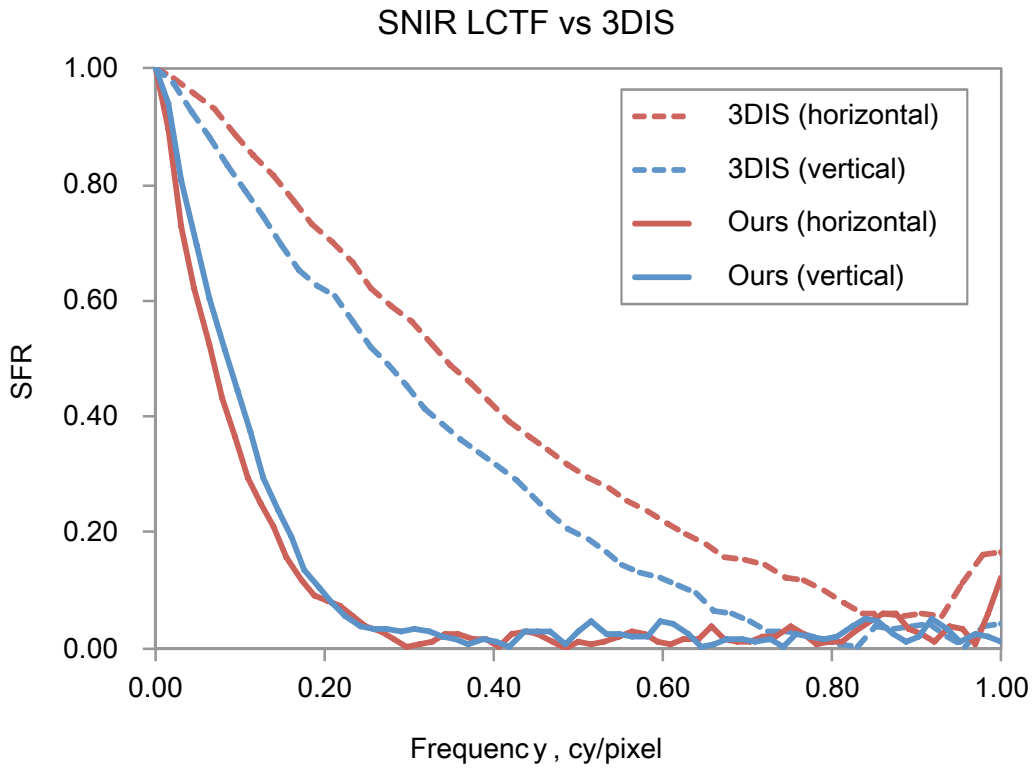

(b)

Figure 5.6: *(a) presents the measured frequency response of the imager via the VIS LCTF, compared to 3DIS [19]. (b) shows the response via the SNIR LCTF.*

5.4 Perceptual Color Difference

We present the evaluation result for perceptual color difference between the hyperspectral image and the reference measurement in Table 5.1. Perceptual difference of colors, which can be regarded as a Euclidean distance in the CIEUCS and therefore denoted as $\Delta u'v'$, is calculated for each color patch. Table 5.1 shows that the mean and standard deviation of $\Delta u'v'$ values are enoughly small to demonstrate the accuracy of our imaging system as the range of u' and v' coordinates are limited to 0.7.

	Training	Test
Mean $\Delta u'v'$	0.0210	0.0444
Stdev	0.0141	0.0208

Table 5.1: *The mean and standard deviation of $\Delta u'v'$, calculated for both training and test color sets. Regarding that the maximum value of u' and v' are 0.7, the perceptual difference between the color calibration result and the reference measurement is considerably small.*

6. Discussion and Future Work

In this thesis, we proposed a two-way hyperspectral imaging system with multiple polarizing equipments. With this imager, it is possible to obtain a hyperspectral image consists of 101 spectral channels where the spectrum is from visible light to near infrared. This proposed two-way design using a polarizing beam splitter eliminated concerns for exchanging LCTF, which requires accurate positioning and longer acquisition time. Since the polarizations of the light of each way are different to each other, one of the LCTFs is required to be rotated by 90 degrees to transmit the light to a camera.

Our system uses a Cooke-triplet lens to collimate the light focused by the apochromatic lens in the current system. However, the small difference between the focal length of these two lenses yields imperfect parallel beams. Furthermore, it may suffer from spherical aberration. This difference and possibly underlying aberration issue appeared as insignificant blur around the edges of an image, results in low SFR. Using multiple lenses, instead of a single Cooke-triplet, will hopefully match the focal length of the preceding lens and thus might alleviate the blur. We will resolve this issue in our future work.

There is another analysis for the reason of low SFR: it may result from the absence of a post-processing step. Several work related to hyperspectral imaging include a post image processing step to enhance the spatial resolution of their imaging system [2, 19]. Our system, however, does not encompass such process as we concentrated more on the handling of multiple polarizing instruments while covering broad spectrum. In our future work, adapting the super-resolution image formation method in [2] could be possible. We expect that it greatly expands the spatial resolution of our system.

As the beam splitter in our system polarizes the incident light when it splits the light into two directions, capturing a hyperspectral image of already polarized light is unrealizable. Therefore, specular reflection on an object can be partially omitted as it cannot pass through both directions. The problem cannot be solved without substituting all polarization based equipments to non-polarizing equipments. A dichroic mirror could be an alternative for the polarizing beam splitter as it passes the light if its wavelength is longer than the mirror's predefined, standard wavelength and reflects otherwise. However, the alternatives for LCTF are unavailable for now as the LCTF provides incomparable quick selection of narrow spectral bands.

On the other hand, low transmittance of LCTF gives cause for longer shutter speed ($\sim$1.5 s) and results in incapability for capturing dynamic objects. We expect that the total acquisition time could be reduced by applying one or more of these methods: employing a brighter light source to shorten the shutter speed, using aforementioned dichroic mirror to increase the amount of light comes to LCTFs,

designing four-way imaging system to reduce the number of images to be taken from each camera. We leave this as our future work.

Besides these limitations, the radiometric accuracy and the number of channels of our hyperspectral imaging system are noticeably improved, compared to previous multi- or hyperspectral imagers. Furthermore, the two-way design enables us to obtain images from both cameras simultaneously. In this respect, we strongly believe that our system could be beneficial for various applications of hyperspectral imaging, such as medical science or food examination.

7. Conclusion

We have presented a two-way hyperspectral imaging system with two LCTFs. The system allows us to measure physically-meaningful hyperspectral radiance on static objects as two-dimensional radiance maps. We have explained the polarized light path in our system and how we dealt with the issue that arose from using multiple polarization equipments. The radiometric and geometric calibration processes have been described to validate the accuracy of our system. We also have quantitatively evaluated the accuracy of this proposed imaging system in terms of radiometry and spatial frequency response and compared the imaging performance of our system with prior works.

Appendices

Appendix A. Calibration Data

Color patches												
Wave-length	#1	#2	#3	#4	#5	#6	#7	#8	#9	#10	#11	#12
400	0.0025	0.0043	0.0020	0.0008	0.0050	0.0036	0.0063	0.0010	0.0014	0.0040	0.0057	0.0014
407	0.0039	0.0061	0.0032	0.0012	0.0075	0.0053	0.0087	0.0016	0.0022	0.0056	0.0079	0.0021
414	0.0041	0.0075	0.0029	0.0009	0.0073	0.0053	0.0103	0.0015	0.0019	0.0053	0.0093	0.0025
421	0.0046	0.0059	0.0033	0.0009	0.0070	0.0045	0.0081	0.0015	0.0017	0.0044	0.0072	0.0027
428	0.0052	0.0043	0.0043	0.0008	0.0077	0.0038	0.0084	0.0015	0.0016	0.0047	0.0054	0.0028
435	0.0051	0.0041	0.0042	0.0007	0.0074	0.0032	0.0083	0.0014	0.0014	0.0037	0.0050	0.0030
442	0.0061	0.0030	0.0053	0.0007	0.0085	0.0029	0.0079	0.0016	0.0014	0.0039	0.0037	0.0035
449	0.0065	0.0035	0.0055	0.0006	0.0086	0.0029	0.0086	0.0016	0.0014	0.0034	0.0041	0.0034
456	0.0080	0.0022	0.0072	0.0006	0.0089	0.0024	0.0072	0.0017	0.0013	0.0032	0.0026	0.0036
463	0.0098	0.0024	0.0087	0.0006	0.0104	0.0026	0.0074	0.0019	0.0015	0.0034	0.0028	0.0045
470	0.0133	0.0027	0.0118	0.0008	0.0122	0.0034	0.0087	0.0024	0.0020	0.0038	0.0033	0.0057
477	0.0188	0.0036	0.0164	0.0011	0.0152	0.0050	0.0102	0.0031	0.0027	0.0043	0.0042	0.0073
484	0.0228	0.0048	0.0191	0.0013	0.0166	0.0067	0.0108	0.0039	0.0036	0.0046	0.0057	0.0093
491	0.0269	0.0059	0.0213	0.0015	0.0180	0.0100	0.0116	0.0047	0.0049	0.0051	0.0087	0.0106
498	0.0306	0.0065	0.0232	0.0016	0.0184	0.0135	0.0114	0.0051	0.0053	0.0049	0.0113	0.0115
505	0.0333	0.0073	0.0235	0.0017	0.0178	0.0180	0.0107	0.0053	0.0059	0.0045	0.0149	0.0118
512	0.0329	0.0082	0.0217	0.0017	0.0166	0.0229	0.0101	0.0054	0.0069	0.0043	0.0206	0.0121
519	0.0328	0.0102	0.0202	0.0017	0.0157	0.0280	0.0088	0.0058	0.0084	0.0039	0.0269	0.0124
526	0.0334	0.0151	0.0187	0.0019	0.0153	0.0326	0.0082	0.0060	0.0103	0.0038	0.0335	0.0129
533	0.0336	0.0208	0.0173	0.0020	0.0153	0.0355	0.0081	0.0063	0.0119	0.0040	0.0392	0.0134
540	0.0338	0.0258	0.0156	0.0021	0.0156	0.0380	0.0076	0.0065	0.0128	0.0040	0.0449	0.0141
547	0.0337	0.0296	0.0140	0.0022	0.0160	0.0402	0.0080	0.0067	0.0129	0.0042	0.0494	0.0146
554	0.0342	0.0338	0.0127	0.0023	0.0166	0.0425	0.0086	0.0071	0.0127	0.0043	0.0546	0.0157
561	0.0334	0.0366	0.0112	0.0024	0.0160	0.0427	0.0086	0.0073	0.0121	0.0043	0.0575	0.0163
568	0.0321	0.0401	0.0100	0.0025	0.0156	0.0426	0.0093	0.0076	0.0114	0.0045	0.0603	0.0168
575	0.0329	0.0464	0.0098	0.0027	0.0171	0.0458	0.0116	0.0086	0.0120	0.0054	0.0683	0.0188
582	0.0312	0.0507	0.0093	0.0030	0.0181	0.0453	0.0151	0.0091	0.0119	0.0061	0.0713	0.0198
589	0.0280	0.0530	0.0086	0.0030	0.0193	0.0418	0.0203	0.0091	0.0114	0.0069	0.0711	0.0197
596	0.0265	0.0593	0.0088	0.0033	0.0219	0.0406	0.0294	0.0098	0.0117	0.0087	0.0761	0.0210
603	0.0276	0.0699	0.0096	0.0038	0.0268	0.0426	0.0426	0.0111	0.0132	0.0110	0.0880	0.0243
610	0.0270	0.0749	0.0097	0.0040	0.0297	0.0419	0.0545	0.0117	0.0140	0.0127	0.0934	0.0257

Table 8.1: *Average intensities of an X-Rite Mini ColorChecker (#1 - #12) for a wavelength range 400–610 nm, measured with our hyperspectral imaging system.*

Color patches												
Wave-length	#1	#2	#3	#4	#5	#6	#7	#8	#9	#10	#11	#12
617	0.0254	0.0750	0.0095	0.0040	0.0298	0.0401	0.0622	0.0117	0.0140	0.0135	0.0939	0.0257
624	0.0249	0.0759	0.0094	0.0040	0.0303	0.0397	0.0692	0.0118	0.0144	0.0141	0.0963	0.0260
631	0.0250	0.0779	0.0096	0.0041	0.0321	0.0405	0.0762	0.0120	0.0153	0.0152	0.0998	0.0265
638	0.0250	0.0799	0.0098	0.0042	0.0351	0.0410	0.0845	0.0123	0.0163	0.0163	0.1034	0.0272
645	0.0256	0.0837	0.0103	0.0043	0.0397	0.0421	0.0943	0.0128	0.0172	0.0176	0.1075	0.0282
652	0.0266	0.0884	0.0119	0.0053	0.0442	0.0428	0.1032	0.0137	0.0180	0.0182	0.1082	0.0288
659	0.0280	0.0918	0.0125	0.0054	0.0508	0.0451	0.1118	0.0140	0.0190	0.0202	0.1117	0.0294
666	0.0294	0.0946	0.0130	0.0056	0.0569	0.0477	0.1196	0.0144	0.0197	0.0224	0.1152	0.0302
673	0.0321	0.0996	0.0137	0.0058	0.0622	0.0523	0.1280	0.0148	0.0204	0.0258	0.1177	0.0312
680	0.0340	0.1010	0.0138	0.0059	0.0642	0.0549	0.1320	0.0150	0.0201	0.0287	0.1158	0.0317
687	0.0357	0.1026	0.0138	0.0062	0.0648	0.0576	0.1357	0.0153	0.0197	0.0325	0.1161	0.0322
694	0.0382	0.1058	0.0139	0.0062	0.0667	0.0607	0.1396	0.0155	0.0198	0.0376	0.1204	0.0324
701	0.0397	0.1087	0.0139	0.0064	0.0685	0.0638	0.1450	0.0157	0.0201	0.0434	0.1275	0.0330
708	0.0405	0.1102	0.0138	0.0065	0.0711	0.0650	0.1480	0.0158	0.0207	0.0498	0.1316	0.0332
715	0.0402	0.1120	0.0141	0.0067	0.0737	0.0645	0.1511	0.0160	0.0212	0.0550	0.1345	0.0335
722	0.0394	0.1123	0.0147	0.0068	0.0769	0.0635	0.1527	0.0162	0.0219	0.0601	0.1366	0.0338
729	0.0390	0.1127	0.0158	0.0069	0.0807	0.0634	0.1544	0.0162	0.0225	0.0644	0.1380	0.0337
736	0.0398	0.1133	0.0175	0.0068	0.0859	0.0652	0.1549	0.0161	0.0234	0.0690	0.1389	0.0334
743	0.0420	0.1135	0.0202	0.0069	0.0938	0.0685	0.1555	0.0160	0.0250	0.0739	0.1396	0.0333
750	0.0432	0.1100	0.0233	0.0067	0.1006	0.0698	0.1508	0.0155	0.0261	0.0767	0.1363	0.0321
757	0.0480	0.1164	0.0304	0.0071	0.1161	0.0773	0.1604	0.0164	0.0293	0.0858	0.1455	0.0341
764	0.0517	0.1224	0.0379	0.0074	0.1302	0.0835	0.1692	0.0173	0.0320	0.0941	0.1531	0.0356
771	0.0509	0.1191	0.0414	0.0073	0.1329	0.0820	0.1652	0.0168	0.0318	0.0947	0.1491	0.0344
778	0.0477	0.1111	0.0410	0.0068	0.1295	0.0768	0.1546	0.0157	0.0305	0.0924	0.1393	0.0320
785	0.0479	0.1100	0.0417	0.0066	0.1324	0.0769	0.1525	0.0153	0.0307	0.0958	0.1377	0.0312
792	0.0477	0.1071	0.0423	0.0064	0.1325	0.0767	0.1493	0.0149	0.0302	0.0979	0.1348	0.0302
799	0.0479	0.1024	0.0429	0.0062	0.1292	0.0764	0.1432	0.0143	0.0291	0.0975	0.1296	0.0289
806	0.0494	0.0982	0.0439	0.0060	0.1259	0.0774	0.1377	0.0139	0.0282	0.0971	0.1249	0.0279
813	0.0521	0.0963	0.0462	0.0059	0.1242	0.0802	0.1357	0.0136	0.0275	0.0976	0.1231	0.0273
820	0.0552	0.0937	0.0485	0.0058	0.1225	0.0830	0.1329	0.0133	0.0269	0.0976	0.1204	0.0267
827	0.0553	0.0872	0.0480	0.0054	0.1147	0.0820	0.1246	0.0124	0.0252	0.0936	0.1139	0.0251
834	0.0577	0.0843	0.0490	0.0052	0.1110	0.0827	0.1194	0.0118	0.0243	0.0914	0.1089	0.0237
841	0.0605	0.0823	0.0503	0.0051	0.1080	0.0837	0.1159	0.0112	0.0235	0.0895	0.1052	0.0228
848	0.0613	0.0783	0.0500	0.0048	0.1036	0.0824	0.1107	0.0107	0.0224	0.0863	0.1006	0.0218
855	0.0601	0.0723	0.0478	0.0045	0.0975	0.0788	0.1028	0.0100	0.0212	0.0818	0.0944	0.0204

Table 8.2: *Average intensities of an X-Rite Mini ColorChecker (#1 - #12) for a wavelength range 617–855 nm, measured with our hyperspectral imaging system.*

Color patches												
Wave-length	#1	#2	#3	#4	#5	#6	#7	#8	#9	#10	#11	#12
862	0.0595	0.0688	0.0467	0.0043	0.0922	0.0763	0.0979	0.0095	0.0200	0.0781	0.0900	0.0194
869	0.0591	0.0660	0.0457	0.0040	0.0882	0.0739	0.0930	0.0089	0.0188	0.0747	0.0850	0.0181
876	0.0567	0.0616	0.0431	0.0037	0.0825	0.0698	0.0864	0.0082	0.0175	0.0700	0.0787	0.0165
883	0.0571	0.0612	0.0434	0.0037	0.0820	0.0704	0.0865	0.0082	0.0174	0.0708	0.0793	0.0165
890	0.0669	0.0699	0.0502	0.0041	0.0940	0.0810	0.0993	0.0094	0.0198	0.0813	0.0908	0.0189
897	0.0720	0.0741	0.0531	0.0043	0.0995	0.0857	0.1040	0.0099	0.0208	0.0860	0.0952	0.0197
904	0.0418	0.0429	0.0308	0.0025	0.0572	0.0498	0.0601	0.0057	0.0119	0.0501	0.0551	0.0114
911	0.0484	0.0496	0.0358	0.0029	0.0658	0.0577	0.0697	0.0067	0.0137	0.0583	0.0638	0.0132
918	0.0441	0.0450	0.0325	0.0026	0.0596	0.0526	0.0631	0.0060	0.0124	0.0531	0.0578	0.0119
925	0.0393	0.0400	0.0291	0.0023	0.0530	0.0468	0.0560	0.0054	0.0110	0.0476	0.0513	0.0104
932	0.0346	0.0349	0.0256	0.0020	0.0464	0.0408	0.0490	0.0047	0.0095	0.0415	0.0448	0.0091
939	0.0308	0.0309	0.0227	0.0018	0.0412	0.0361	0.0432	0.0041	0.0083	0.0369	0.0396	0.0079
946	0.0177	0.0176	0.0129	0.0010	0.0236	0.0207	0.0245	0.0023	0.0047	0.0212	0.0225	0.0044
953	0.0183	0.0183	0.0135	0.0010	0.0244	0.0215	0.0255	0.0024	0.0049	0.0221	0.0234	0.0046
960	0.0182	0.0181	0.0134	0.0010	0.0241	0.0213	0.0253	0.0024	0.0048	0.0218	0.0231	0.0046
967	0.0171	0.0171	0.0126	0.0009	0.0223	0.0199	0.0235	0.0022	0.0045	0.0204	0.0215	0.0042
974	0.0166	0.0166	0.0123	0.0009	0.0217	0.0192	0.0228	0.0020	0.0043	0.0198	0.0207	0.0041
981	0.0141	0.0141	0.0104	0.0007	0.0185	0.0165	0.0194	0.0017	0.0037	0.0170	0.0177	0.0035
988	0.0127	0.0127	0.0093	0.0006	0.0166	0.0147	0.0174	0.0015	0.0033	0.0152	0.0159	0.0031
995	0.0093	0.0093	0.0068	0.0005	0.0121	0.0108	0.0128	0.0011	0.0024	0.0112	0.0116	0.0023
1002	0.0074	0.0073	0.0055	0.0004	0.0096	0.0086	0.0102	0.0009	0.0019	0.0090	0.0093	0.0018
1009	0.0076	0.0076	0.0056	0.0004	0.0100	0.0089	0.0106	0.0009	0.0019	0.0093	0.0097	0.0018
1016	0.0077	0.0077	0.0055	0.0004	0.0100	0.0089	0.0105	0.0009	0.0019	0.0094	0.0096	0.0018
1023	0.0088	0.0087	0.0064	0.0005	0.0116	0.0102	0.0121	0.0010	0.0022	0.0109	0.0111	0.0020
1030	0.0025	0.0025	0.0018	0.0001	0.0033	0.0029	0.0035	0.0003	0.0006	0.0031	0.0031	0.0006
1037	0.0025	0.0025	0.0019	0.0001	0.0033	0.0029	0.0035	0.0003	0.0006	0.0031	0.0032	0.0005
1044	0.0018	0.0019	0.0014	0.0001	0.0024	0.0021	0.0025	0.0002	0.0004	0.0023	0.0023	0.0004
1051	0.0013	0.0013	0.0009	0.0001	0.0017	0.0015	0.0018	0.0001	0.0003	0.0016	0.0017	0.0003
1058	0.0009	0.0009	0.0006	0.0001	0.0012	0.0011	0.0013	0.0001	0.0002	0.0011	0.0012	0.0002
1065	0.0006	0.0006	0.0004	0.0000	0.0008	0.0007	0.0009	0.0001	0.0001	0.0007	0.0008	0.0001
1072	0.0004	0.0004	0.0002	0.0000	0.0005	0.0004	0.0006	0.0000	0.0001	0.0005	0.0005	0.0001
1079	0.0002	0.0003	0.0001	0.0000	0.0003	0.0003	0.0003	0.0000	0.0001	0.0003	0.0003	0.0001
1086	0.0001	0.0001	0.0001	0.0000	0.0002	0.0002	0.0002	0.0000	0.0000	0.0002	0.0002	0.0000
1093	0.0001	0.0001	0.0000	0.0000	0.0001	0.0001	0.0001	0.0000	0.0000	0.0001	0.0001	0.0000
1100	0.0001	0.0001	0.0000	0.0000	0.0001	0.0001	0.0001	0.0000	0.0000	0.0001	0.0001	0.0000

Table 8.3: *Average intensities of an X-Rite Mini ColorChecker (#1 - #12) for a wavelength range 862–1100 nm, measured with our hyperspectral imaging system.*

Color patches												
Wave-length	#1	#2	#3	#4	#5	#6	#7	#8	#9	#10	#11	#12
400	0.0019	0.0041	0.0046	0.0024	0.0059	0.0036	0.0022	0.0040	0.0021	0.0049	0.0023	0.0062
407	0.0030	0.0055	0.0063	0.0034	0.0083	0.0049	0.0034	0.0054	0.0032	0.0068	0.0034	0.0086
414	0.0031	0.0070	0.0071	0.0048	0.0091	0.0050	0.0028	0.0080	0.0028	0.0077	0.0029	0.0120
421	0.0036	0.0053	0.0046	0.0052	0.0071	0.0050	0.0026	0.0087	0.0025	0.0060	0.0034	0.0132
428	0.0045	0.0047	0.0040	0.0056	0.0062	0.0061	0.0026	0.0094	0.0022	0.0046	0.0043	0.0148
435	0.0043	0.0046	0.0039	0.0058	0.0058	0.0057	0.0020	0.0107	0.0020	0.0041	0.0041	0.0162
442	0.0055	0.0040	0.0030	0.0070	0.0056	0.0079	0.0022	0.0128	0.0019	0.0032	0.0053	0.0195
449	0.0054	0.0042	0.0032	0.0075	0.0061	0.0074	0.0019	0.0125	0.0017	0.0033	0.0049	0.0184
456	0.0062	0.0032	0.0020	0.0077	0.0053	0.0082	0.0020	0.0134	0.0016	0.0022	0.0063	0.0199
463	0.0073	0.0035	0.0021	0.0094	0.0066	0.0100	0.0024	0.0159	0.0018	0.0024	0.0073	0.0234
470	0.0094	0.0044	0.0024	0.0116	0.0085	0.0113	0.0031	0.0190	0.0020	0.0027	0.0086	0.0289
477	0.0116	0.0052	0.0027	0.0151	0.0115	0.0133	0.0048	0.0249	0.0025	0.0035	0.0101	0.0378
484	0.0134	0.0060	0.0033	0.0178	0.0150	0.0143	0.0069	0.0304	0.0030	0.0046	0.0103	0.0457
491	0.0149	0.0069	0.0042	0.0205	0.0182	0.0143	0.0100	0.0346	0.0038	0.0056	0.0095	0.0513
498	0.0150	0.0071	0.0042	0.0221	0.0200	0.0130	0.0129	0.0367	0.0039	0.0057	0.0080	0.0543
505	0.0148	0.0070	0.0040	0.0229	0.0215	0.0117	0.0164	0.0380	0.0042	0.0061	0.0069	0.0569
512	0.0144	0.0071	0.0042	0.0236	0.0220	0.0107	0.0202	0.0395	0.0046	0.0072	0.0059	0.0593
519	0.0140	0.0069	0.0040	0.0243	0.0205	0.0096	0.0226	0.0407	0.0050	0.0083	0.0051	0.0611
526	0.0136	0.0071	0.0046	0.0248	0.0187	0.0087	0.0237	0.0414	0.0053	0.0101	0.0046	0.0613
533	0.0134	0.0074	0.0049	0.0256	0.0177	0.0082	0.0237	0.0425	0.0055	0.0119	0.0043	0.0621
540	0.0137	0.0073	0.0047	0.0270	0.0177	0.0079	0.0241	0.0447	0.0057	0.0132	0.0042	0.0652
547	0.0140	0.0076	0.0048	0.0280	0.0191	0.0078	0.0239	0.0464	0.0061	0.0146	0.0042	0.0674
554	0.0142	0.0082	0.0050	0.0296	0.0205	0.0078	0.0236	0.0491	0.0065	0.0168	0.0041	0.0700
561	0.0139	0.0086	0.0050	0.0307	0.0207	0.0075	0.0222	0.0499	0.0066	0.0186	0.0039	0.0688
568	0.0134	0.0095	0.0055	0.0316	0.0209	0.0072	0.0200	0.0495	0.0069	0.0214	0.0037	0.0661
575	0.0142	0.0119	0.0066	0.0347	0.0248	0.0076	0.0195	0.0534	0.0082	0.0276	0.0039	0.0707
582	0.0141	0.0158	0.0079	0.0357	0.0292	0.0076	0.0175	0.0546	0.0093	0.0343	0.0040	0.0743
589	0.0138	0.0222	0.0103	0.0355	0.0350	0.0078	0.0153	0.0556	0.0106	0.0420	0.0042	0.0787
596	0.0146	0.0331	0.0158	0.0384	0.0436	0.0086	0.0145	0.0612	0.0129	0.0535	0.0047	0.0899
603	0.0168	0.0489	0.0267	0.0451	0.0572	0.0103	0.0153	0.0735	0.0163	0.0695	0.0056	0.1100
610	0.0179	0.0618	0.0405	0.0485	0.0666	0.0114	0.0153	0.0797	0.0185	0.0781	0.0061	0.1193

Table 8.4: *Average intensities of an X-Rite Mini ColorChecker (#13 - #24) for a wavelength range 400–610 nm, measured with our hyperspectral imaging system.*

Color patches												
Wave-length	#1	#2	#3	#4	#5	#6	#7	#8	#9	#10	#11	#12
617	0.0178	0.0688	0.0529	0.0488	0.0698	0.0116	0.0145	0.0795	0.0187	0.0779	0.0062	0.1179
624	0.0177	0.0736	0.0640	0.0493	0.0727	0.0118	0.0143	0.0802	0.0194	0.0779	0.0063	0.1182
631	0.0183	0.0781	0.0731	0.0500	0.0771	0.0126	0.0145	0.0819	0.0208	0.0798	0.0066	0.1212
638	0.0190	0.0816	0.0800	0.0516	0.0812	0.0134	0.0146	0.0844	0.0224	0.0816	0.0070	0.1257
645	0.0204	0.0854	0.0859	0.0538	0.0865	0.0147	0.0149	0.0880	0.0245	0.0841	0.0074	0.1321
652	0.0204	0.0839	0.0872	0.0537	0.0879	0.0155	0.0152	0.0884	0.0252	0.0832	0.0077	0.1345
659	0.0224	0.0876	0.0909	0.0551	0.0946	0.0174	0.0157	0.0913	0.0274	0.0867	0.0085	0.1392
666	0.0241	0.0904	0.0948	0.0572	0.1003	0.0195	0.0164	0.0934	0.0286	0.0898	0.0091	0.1436
673	0.0254	0.0948	0.0995	0.0590	0.1079	0.0226	0.0178	0.0964	0.0297	0.0951	0.0097	0.1485
680	0.0255	0.0962	0.1014	0.0600	0.1117	0.0254	0.0189	0.0978	0.0291	0.0973	0.0100	0.1506
687	0.0253	0.0976	0.1040	0.0612	0.1155	0.0285	0.0202	0.0985	0.0287	0.1001	0.0105	0.1530
694	0.0252	0.0986	0.1049	0.0612	0.1230	0.0331	0.0217	0.1000	0.0289	0.1040	0.0112	0.1551
701	0.0250	0.1011	0.1080	0.0624	0.1300	0.0389	0.0233	0.1026	0.0298	0.1094	0.0121	0.1592
708	0.0249	0.1027	0.1092	0.0630	0.1371	0.0449	0.0239	0.1036	0.0310	0.1128	0.0130	0.1608
715	0.0251	0.1022	0.1096	0.0630	0.1403	0.0510	0.0236	0.1039	0.0323	0.1134	0.0139	0.1617
722	0.0263	0.1027	0.1108	0.0637	0.1437	0.0578	0.0232	0.1055	0.0338	0.1141	0.0154	0.1645
729	0.0280	0.1028	0.1114	0.0636	0.1441	0.0638	0.0230	0.1049	0.0354	0.1143	0.0171	0.1644
736	0.0310	0.1038	0.1129	0.0638	0.1443	0.0700	0.0237	0.1037	0.0378	0.1161	0.0198	0.1642
743	0.0350	0.1043	0.1137	0.0638	0.1466	0.0761	0.0254	0.1040	0.0423	0.1194	0.0239	0.1664
750	0.0388	0.1013	0.1103	0.0614	0.1449	0.0791	0.0270	0.1013	0.0454	0.1183	0.0285	0.1624
757	0.0460	0.1075	0.1177	0.0657	0.1538	0.0882	0.0314	0.1087	0.0527	0.1276	0.0369	0.1745
764	0.0514	0.1123	0.1233	0.0685	0.1606	0.0953	0.0346	0.1130	0.0596	0.1352	0.0457	0.1821
771	0.0518	0.1087	0.1199	0.0663	0.1565	0.0947	0.0344	0.1097	0.0608	0.1322	0.0506	0.1766
778	0.0494	0.1009	0.1114	0.0615	0.1482	0.0906	0.0324	0.1022	0.0598	0.1246	0.0531	0.1640
785	0.0492	0.0996	0.1098	0.0599	0.1470	0.0916	0.0327	0.1009	0.0607	0.1246	0.0586	0.1616
792	0.0485	0.0975	0.1076	0.0582	0.1433	0.0902	0.0333	0.0976	0.0607	0.1239	0.0627	0.1569
799	0.0466	0.0941	0.1042	0.0561	0.1366	0.0869	0.0348	0.0930	0.0587	0.1208	0.0652	0.1509
806	0.0452	0.0906	0.1008	0.0543	0.1319	0.0846	0.0377	0.0903	0.0568	0.1186	0.0672	0.1464
813	0.0441	0.0888	0.0995	0.0533	0.1298	0.0838	0.0424	0.0891	0.0559	0.1185	0.0696	0.1451
820	0.0431	0.0865	0.0972	0.0522	0.1263	0.0821	0.0476	0.0874	0.0540	0.1167	0.0706	0.1425
827	0.0403	0.0817	0.0924	0.0494	0.1175	0.0778	0.0513	0.0822	0.0498	0.1100	0.0685	0.1339
834	0.0391	0.0789	0.0888	0.0469	0.1140	0.0754	0.0555	0.0776	0.0484	0.1076	0.0676	0.1274
841	0.0377	0.0758	0.0855	0.0447	0.1098	0.0732	0.0597	0.0743	0.0466	0.1045	0.0669	0.1226
848	0.0356	0.0717	0.0811	0.0426	0.1052	0.0707	0.0630	0.0718	0.0438	0.0992	0.0651	0.1175
855	0.0338	0.0674	0.0762	0.0400	0.1008	0.0678	0.0646	0.0681	0.0417	0.0944	0.0627	0.1114

Table 8.5: *Average intensities of an X-Rite Mini ColorChecker (#13 - #24) for a wavelength range 617–855 nm, measured with our hyperspectral imaging system.*

Color patches												
Wave-length	#1	#2	#3	#4	#5	#6	#7	#8	#9	#10	#11	#12
862	0.0321	0.0645	0.0730	0.0384	0.0953	0.0650	0.0655	0.0653	0.0399	0.0908	0.0611	0.1073
869	0.0303	0.0607	0.0689	0.0360	0.0907	0.0622	0.0650	0.0610	0.0382	0.0866	0.0588	0.1012
876	0.0281	0.0562	0.0634	0.0326	0.0840	0.0581	0.0621	0.0554	0.0354	0.0797	0.0545	0.0918
883	0.0281	0.0564	0.0640	0.0329	0.0835	0.0584	0.0641	0.0559	0.0352	0.0789	0.0549	0.0914
890	0.0323	0.0645	0.0735	0.0378	0.0965	0.0683	0.0757	0.0643	0.0410	0.0909	0.0643	0.1058
897	0.0340	0.0676	0.0771	0.0393	0.1013	0.0726	0.0812	0.0675	0.0437	0.0960	0.0686	0.1120
904	0.0196	0.0392	0.0448	0.0228	0.0584	0.0423	0.0475	0.0390	0.0256	0.0555	0.0402	0.0646
911	0.0226	0.0454	0.0521	0.0265	0.0669	0.0492	0.0555	0.0448	0.0300	0.0641	0.0469	0.0743
918	0.0205	0.0412	0.0474	0.0239	0.0599	0.0445	0.0500	0.0397	0.0275	0.0576	0.0423	0.0662
925	0.0183	0.0367	0.0421	0.0211	0.0533	0.0399	0.0447	0.0350	0.0250	0.0513	0.0380	0.0585
932	0.0159	0.0317	0.0366	0.0184	0.0472	0.0355	0.0397	0.0309	0.0227	0.0452	0.0338	0.0518
939	0.0140	0.0279	0.0323	0.0163	0.0419	0.0318	0.0354	0.0274	0.0204	0.0400	0.0302	0.0462
946	0.0080	0.0158	0.0183	0.0091	0.0239	0.0183	0.0203	0.0155	0.0118	0.0227	0.0173	0.0260
953	0.0082	0.0164	0.0191	0.0095	0.0246	0.0192	0.0211	0.0161	0.0125	0.0233	0.0180	0.0268
960	0.0081	0.0162	0.0187	0.0093	0.0242	0.0191	0.0210	0.0159	0.0125	0.0227	0.0179	0.0264
967	0.0075	0.0149	0.0174	0.0086	0.0224	0.0179	0.0196	0.0147	0.0120	0.0212	0.0168	0.0245
974	0.0073	0.0145	0.0169	0.0083	0.0220	0.0178	0.0191	0.0143	0.0120	0.0208	0.0166	0.0238
981	0.0061	0.0124	0.0144	0.0070	0.0187	0.0153	0.0165	0.0122	0.0105	0.0178	0.0143	0.0204
988	0.0054	0.0110	0.0129	0.0062	0.0166	0.0136	0.0146	0.0109	0.0094	0.0158	0.0128	0.0182
995	0.0040	0.0080	0.0095	0.0046	0.0120	0.0100	0.0107	0.0079	0.0070	0.0114	0.0094	0.0133
1002	0.0032	0.0064	0.0076	0.0037	0.0096	0.0080	0.0086	0.0063	0.0057	0.0092	0.0075	0.0105
1009	0.0034	0.0067	0.0079	0.0038	0.0100	0.0084	0.0089	0.0065	0.0060	0.0095	0.0079	0.0110
1016	0.0034	0.0066	0.0079	0.0039	0.0100	0.0085	0.0089	0.0064	0.0061	0.0096	0.0080	0.0110
1023	0.0039	0.0076	0.0090	0.0044	0.0117	0.0099	0.0103	0.0074	0.0071	0.0111	0.0092	0.0127
1030	0.0011	0.0022	0.0026	0.0012	0.0033	0.0028	0.0029	0.0021	0.0021	0.0032	0.0026	0.0036
1037	0.0011	0.0022	0.0026	0.0012	0.0033	0.0029	0.0029	0.0021	0.0021	0.0031	0.0027	0.0036
1044	0.0008	0.0016	0.0019	0.0009	0.0024	0.0021	0.0021	0.0016	0.0015	0.0023	0.0020	0.0026
1051	0.0005	0.0011	0.0014	0.0006	0.0017	0.0015	0.0015	0.0011	0.0011	0.0016	0.0014	0.0019
1058	0.0004	0.0008	0.0010	0.0005	0.0012	0.0010	0.0011	0.0008	0.0007	0.0012	0.0010	0.0014
1065	0.0002	0.0005	0.0006	0.0003	0.0009	0.0007	0.0007	0.0005	0.0005	0.0008	0.0006	0.0009
1072	0.0002	0.0004	0.0004	0.0002	0.0005	0.0004	0.0004	0.0003	0.0003	0.0005	0.0004	0.0006
1079	0.0001	0.0002	0.0003	0.0001	0.0003	0.0003	0.0003	0.0002	0.0002	0.0003	0.0002	0.0004
1086	0.0001	0.0001	0.0001	0.0001	0.0002	0.0002	0.0001	0.0001	0.0001	0.0002	0.0001	0.0002
1093	0.0000	0.0001	0.0001	0.0000	0.0001	0.0001	0.0001	0.0000	0.0000	0.0001	0.0001	0.0001
1100	0.0000	0.0001	0.0001	0.0000	0.0001	0.0001	0.0001	0.0000	0.0000	0.0001	0.0001	0.0001

Table 8.6: *Average intensities of an X-Rite Mini ColorChecker (#13 - #24) for a wavelength range 862–1100 nm, measured with our hyperspectral imaging system.*

Color patches												
Wave-length	#1	#2	#3	#4	#5	#6	#7	#8	#9	#10	#11	#12
400	0.0035	0.0007	0.0029	0.0002	0.0040	0.0010	0.0043	0.0011	0.0006	0.0023	0.0010	0.0025
407	0.0048	0.0011	0.0042	0.0005	0.0061	0.0014	0.0063	0.0016	0.0009	0.0030	0.0013	0.0034
414	0.0055	0.0011	0.0049	0.0005	0.0072	0.0014	0.0071	0.0017	0.0008	0.0033	0.0013	0.0037
421	0.0061	0.0011	0.0054	0.0006	0.0078	0.0015	0.0075	0.0019	0.0010	0.0035	0.0015	0.0039
428	0.0065	0.0012	0.0059	0.0007	0.0084	0.0016	0.0079	0.0020	0.0011	0.0036	0.0016	0.0042
435	0.0072	0.0013	0.0066	0.0007	0.0089	0.0016	0.0080	0.0021	0.0011	0.0035	0.0016	0.0046
442	0.0081	0.0015	0.0077	0.0008	0.0096	0.0019	0.0083	0.0024	0.0013	0.0037	0.0018	0.0049
449	0.0084	0.0014	0.0083	0.0008	0.0095	0.0018	0.0077	0.0023	0.0012	0.0033	0.0017	0.0049
456	0.0089	0.0015	0.0087	0.0007	0.0094	0.0019	0.0071	0.0022	0.0012	0.0030	0.0018	0.0049
463	0.0109	0.0018	0.0106	0.0008	0.0105	0.0024	0.0077	0.0026	0.0014	0.0031	0.0021	0.0056
470	0.0141	0.0023	0.0134	0.0010	0.0122	0.0031	0.0085	0.0031	0.0020	0.0034	0.0027	0.0066
477	0.0190	0.0032	0.0176	0.0014	0.0148	0.0045	0.0097	0.0039	0.0028	0.0040	0.0038	0.0083
484	0.0246	0.0043	0.0218	0.0015	0.0172	0.0063	0.0107	0.0045	0.0037	0.0042	0.0051	0.0099
491	0.0300	0.0054	0.0252	0.0019	0.0187	0.0091	0.0112	0.0053	0.0047	0.0043	0.0073	0.0115
498	0.0329	0.0060	0.0261	0.0020	0.0185	0.0123	0.0108	0.0056	0.0052	0.0042	0.0100	0.0121
505	0.0345	0.0065	0.0258	0.0020	0.0178	0.0166	0.0104	0.0058	0.0056	0.0040	0.0139	0.0125
512	0.0354	0.0074	0.0249	0.0021	0.0168	0.0221	0.0099	0.0060	0.0063	0.0038	0.0195	0.0129
519	0.0359	0.0093	0.0233	0.0021	0.0157	0.0278	0.0089	0.0061	0.0075	0.0035	0.0260	0.0132
526	0.0363	0.0133	0.0217	0.0022	0.0150	0.0335	0.0078	0.0064	0.0095	0.0032	0.0339	0.0137
533	0.0366	0.0194	0.0198	0.0022	0.0148	0.0378	0.0072	0.0066	0.0116	0.0031	0.0414	0.0142
540	0.0369	0.0260	0.0179	0.0022	0.0150	0.0410	0.0070	0.0068	0.0125	0.0030	0.0480	0.0147
547	0.0365	0.0313	0.0158	0.0023	0.0154	0.0431	0.0074	0.0071	0.0127	0.0032	0.0536	0.0153
554	0.0363	0.0351	0.0141	0.0025	0.0155	0.0443	0.0081	0.0074	0.0125	0.0035	0.0579	0.0160
561	0.0350	0.0380	0.0121	0.0025	0.0150	0.0445	0.0081	0.0075	0.0116	0.0035	0.0610	0.0164
568	0.0332	0.0410	0.0104	0.0025	0.0145	0.0440	0.0082	0.0077	0.0108	0.0035	0.0633	0.0168
575	0.0336	0.0472	0.0100	0.0028	0.0153	0.0467	0.0099	0.0084	0.0111	0.0041	0.0704	0.0186
582	0.0315	0.0517	0.0091	0.0029	0.0160	0.0456	0.0127	0.0087	0.0109	0.0048	0.0739	0.0194
589	0.0285	0.0547	0.0085	0.0029	0.0170	0.0429	0.0172	0.0089	0.0107	0.0056	0.0750	0.0197
596	0.0272	0.0615	0.0087	0.0032	0.0198	0.0420	0.0260	0.0096	0.0112	0.0073	0.0817	0.0213
603	0.0284	0.0746	0.0094	0.0037	0.0253	0.0448	0.0406	0.0111	0.0127	0.0096	0.0962	0.0249
610	0.0277	0.0814	0.0095	0.0039	0.0290	0.0442	0.0545	0.0118	0.0133	0.0112	0.1025	0.0265

Table 8.7: *Measured radiance values of an X-Rite Mini ColorChecker (#1 - #12) for a wavelength range 400–610 nm, measured with a spectroradiometer.*

Color patches												
Wave-length	#1	#2	#3	#4	#5	#6	#7	#8	#9	#10	#11	#12
400	0.0035	0.0007	0.0029	0.0002	0.0040	0.0010	0.0043	0.0011	0.0006	0.0023	0.0010	0.0025
407	0.0048	0.0011	0.0042	0.0005	0.0061	0.0014	0.0063	0.0016	0.0009	0.0030	0.0013	0.0034
414	0.0055	0.0011	0.0049	0.0005	0.0072	0.0014	0.0071	0.0017	0.0008	0.0033	0.0013	0.0037
421	0.0061	0.0011	0.0054	0.0006	0.0078	0.0015	0.0075	0.0019	0.0010	0.0035	0.0015	0.0039
428	0.0065	0.0012	0.0059	0.0007	0.0084	0.0016	0.0079	0.0020	0.0011	0.0036	0.0016	0.0042
435	0.0072	0.0013	0.0066	0.0007	0.0089	0.0016	0.0080	0.0021	0.0011	0.0035	0.0016	0.0046
442	0.0081	0.0015	0.0077	0.0008	0.0096	0.0019	0.0083	0.0024	0.0013	0.0037	0.0018	0.0049
449	0.0084	0.0014	0.0083	0.0008	0.0095	0.0018	0.0077	0.0023	0.0012	0.0033	0.0017	0.0049
456	0.0089	0.0015	0.0087	0.0007	0.0094	0.0019	0.0071	0.0022	0.0012	0.0030	0.0018	0.0049
463	0.0109	0.0018	0.0106	0.0008	0.0105	0.0024	0.0077	0.0026	0.0014	0.0031	0.0021	0.0056
470	0.0141	0.0023	0.0134	0.0010	0.0122	0.0031	0.0085	0.0031	0.0020	0.0034	0.0027	0.0066
477	0.0190	0.0032	0.0176	0.0014	0.0148	0.0045	0.0097	0.0039	0.0028	0.0040	0.0038	0.0083
484	0.0246	0.0043	0.0218	0.0015	0.0172	0.0063	0.0107	0.0045	0.0037	0.0042	0.0051	0.0099
491	0.0300	0.0054	0.0252	0.0019	0.0187	0.0091	0.0112	0.0053	0.0047	0.0043	0.0073	0.0115
498	0.0329	0.0060	0.0261	0.0020	0.0185	0.0123	0.0108	0.0056	0.0052	0.0042	0.0100	0.0121
505	0.0345	0.0065	0.0258	0.0020	0.0178	0.0166	0.0104	0.0058	0.0056	0.0040	0.0139	0.0125
512	0.0354	0.0074	0.0249	0.0021	0.0168	0.0221	0.0099	0.0060	0.0063	0.0038	0.0195	0.0129
519	0.0359	0.0093	0.0233	0.0021	0.0157	0.0278	0.0089	0.0061	0.0075	0.0035	0.0260	0.0132
526	0.0363	0.0133	0.0217	0.0022	0.0150	0.0335	0.0078	0.0064	0.0095	0.0032	0.0339	0.0137
533	0.0366	0.0194	0.0198	0.0022	0.0148	0.0378	0.0072	0.0066	0.0116	0.0031	0.0414	0.0142
540	0.0369	0.0260	0.0179	0.0022	0.0150	0.0410	0.0070	0.0068	0.0125	0.0030	0.0480	0.0147
547	0.0365	0.0313	0.0158	0.0023	0.0154	0.0431	0.0074	0.0071	0.0127	0.0032	0.0536	0.0153
554	0.0363	0.0351	0.0141	0.0025	0.0155	0.0443	0.0081	0.0074	0.0125	0.0035	0.0579	0.0160
561	0.0350	0.0380	0.0121	0.0025	0.0150	0.0445	0.0081	0.0075	0.0116	0.0035	0.0610	0.0164
568	0.0332	0.0410	0.0104	0.0025	0.0145	0.0440	0.0082	0.0077	0.0108	0.0035	0.0633	0.0168
575	0.0336	0.0472	0.0100	0.0028	0.0153	0.0467	0.0099	0.0084	0.0111	0.0041	0.0704	0.0186
582	0.0315	0.0517	0.0091	0.0029	0.0160	0.0456	0.0127	0.0087	0.0109	0.0048	0.0739	0.0194
589	0.0285	0.0547	0.0085	0.0029	0.0170	0.0429	0.0172	0.0089	0.0107	0.0056	0.0750	0.0197
596	0.0272	0.0615	0.0087	0.0032	0.0198	0.0420	0.0260	0.0096	0.0112	0.0073	0.0817	0.0213
603	0.0284	0.0746	0.0094	0.0037	0.0253	0.0448	0.0406	0.0111	0.0127	0.0096	0.0962	0.0249
610	0.0277	0.0814	0.0095	0.0039	0.0290	0.0442	0.0545	0.0118	0.0133	0.0112	0.1025	0.0265

Table 8.8: *Measured radiance values of an X-Rite Mini ColorChecker (#1 - #12) for a wavelength range 617–855 nm, measured with a spectroradiometer.*

Color patches												
Wave-length	#1	#2	#3	#4	#5	#6	#7	#8	#9	#10	#11	#12
862	0.0612	0.0727	0.0486	0.0032	0.0969	0.0790	0.1046	0.0088	0.0184	0.0795	0.0940	0.0186
869	0.0605	0.0686	0.0473	0.0032	0.0916	0.0761	0.0991	0.0083	0.0171	0.0754	0.0889	0.0176
876	0.0576	0.0640	0.0446	0.0027	0.0851	0.0713	0.0917	0.0073	0.0157	0.0706	0.0831	0.0160
883	0.0582	0.0631	0.0449	0.0033	0.0831	0.0712	0.0904	0.0078	0.0156	0.0698	0.0816	0.0159
890	0.0683	0.0733	0.0527	0.0033	0.0971	0.0832	0.1051	0.0084	0.0179	0.0820	0.0944	0.0179
897	0.0731	0.0762	0.0554	0.0037	0.1015	0.0877	0.1097	0.0095	0.0185	0.0859	0.0983	0.0192
904	0.0597	0.0625	0.0452	0.0030	0.0818	0.0711	0.0888	0.0073	0.0152	0.0706	0.0797	0.0156
911	0.0504	0.0519	0.0377	0.0021	0.0686	0.0604	0.0740	0.0058	0.0124	0.0594	0.0671	0.0125
918	0.0451	0.0466	0.0338	0.0022	0.0614	0.0539	0.0658	0.0054	0.0107	0.0525	0.0598	0.0112
925	0.0409	0.0418	0.0303	0.0018	0.0547	0.0476	0.0586	0.0049	0.0098	0.0469	0.0534	0.0101
932	0.0360	0.0362	0.0270	0.0016	0.0480	0.0416	0.0521	0.0041	0.0082	0.0422	0.0466	0.0086
939	0.0305	0.0311	0.0229	0.0026	0.0396	0.0356	0.0428	0.0045	0.0081	0.0353	0.0387	0.0078
946	0.0192	0.0189	0.0141	0.0001	0.0249	0.0221	0.0268	0.0019	0.0041	0.0217	0.0242	0.0044
953	0.0183	0.0188	0.0138	0.0011	0.0243	0.0214	0.0260	0.0026	0.0044	0.0212	0.0235	0.0045
960	0.0196	0.0196	0.0143	0.0003	0.0254	0.0227	0.0277	0.0017	0.0043	0.0222	0.0245	0.0047
967	0.0186	0.0190	0.0137	0.0000	0.0244	0.0211	0.0268	0.0013	0.0035	0.0214	0.0239	0.0039
974	0.0181	0.0182	0.0128	0.0002	0.0232	0.0203	0.0251	0.0017	0.0036	0.0207	0.0230	0.0037
981	0.0159	0.0162	0.0115	0.0000	0.0206	0.0183	0.0218	0.0008	0.0030	0.0183	0.0198	0.0026
988	0.0140	0.0141	0.0101	0.0001	0.0175	0.0162	0.0198	0.0011	0.0024	0.0162	0.0173	0.0023
995	0.0110	0.0111	0.0079	0.0000	0.0142	0.0127	0.0154	0.0000	0.0010	0.0127	0.0141	0.0013
1002	0.0091	0.0090	0.0062	0.0000	0.0116	0.0103	0.0126	0.0000	0.0004	0.0102	0.0116	0.0007
1009	0.0086	0.0088	0.0060	0.0001	0.0103	0.0099	0.0120	0.0003	0.0017	0.0098	0.0107	0.0015
1016	0.0077	0.0075	0.0056	0.0007	0.0091	0.0078	0.0100	0.0011	0.0020	0.0086	0.0092	0.0020
1023	0.0065	0.0070	0.0049	0.0019	0.0084	0.0075	0.0084	0.0020	0.0025	0.0079	0.0081	0.0026
1030	0.0033	0.0034	0.0019	0.0000	0.0043	0.0044	0.0045	0.0000	0.0000	0.0038	0.0045	0.0000
1037	0.0000	0.0000	0.0000	0.0000	0.0000	0.0000	0.0000	0.0000	0.0000	0.0000	0.0000	0.0000
1044	0.0000	0.0000	0.0000	0.0000	0.0000	0.0000	0.0000	0.0000	0.0000	0.0000	0.0000	0.0000
1051	0.0000	0.0000	0.0000	0.0000	0.0000	0.0000	0.0000	0.0000	0.0000	0.0000	0.0000	0.0000
1058	0.0000	0.0000	0.0000	0.0000	0.0000	0.0000	0.0000	0.0000	0.0000	0.0000	0.0000	0.0000
1065	0.0000	0.0000	0.0000	0.0000	0.0000	0.0000	0.0000	0.0000	0.0000	0.0000	0.0000	0.0000
1072	0.0000	0.0000	0.0000	0.0000	0.0000	0.0000	0.0000	0.0000	0.0000	0.0000	0.0000	0.0000
1079	0.0000	0.0000	0.0000	0.0000	0.0000	0.0000	0.0000	0.0000	0.0000	0.0000	0.0000	0.0000
1086	0.0000	0.0000	0.0000	0.0000	0.0000	0.0000	0.0000	0.0000	0.0000	0.0000	0.0000	0.0000
1093	0.0000	0.0000	0.0000	0.0000	0.0000	0.0000	0.0000	0.0000	0.0000	0.0000	0.0000	0.0000
1100	0.0000	0.0000	0.0000	0.0000	0.0000	0.0000	0.0000	0.0000	0.0000	0.0000	0.0000	0.0000

Table 8.9: *Measured radiance values of an X-Rite Mini ColorChecker (#1 - #12) for a wavelength range 862–1100 nm, measured with a spectroradiometer.*

Color patches												
Wave-length	#1	#2	#3	#4	#5	#6	#7	#8	#9	#10	#11	#12
400	0.0032	0.0021	0.0006	0.0043	0.0023	0.0038	0.0008	0.0059	0.0007	0.0005	0.0024	0.0064
407	0.0048	0.0027	0.0009	0.0062	0.0030	0.0054	0.0012	0.0093	0.0011	0.0008	0.0034	0.0104
414	0.0055	0.0026	0.0008	0.0071	0.0032	0.0062	0.0012	0.0117	0.0010	0.0008	0.0040	0.0147
421	0.0059	0.0028	0.0009	0.0076	0.0034	0.0070	0.0013	0.0131	0.0011	0.0010	0.0045	0.0180
428	0.0064	0.0029	0.0010	0.0081	0.0038	0.0077	0.0015	0.0140	0.0012	0.0011	0.0051	0.0201
435	0.0067	0.0029	0.0011	0.0086	0.0040	0.0084	0.0015	0.0149	0.0012	0.0011	0.0058	0.0220
442	0.0074	0.0033	0.0012	0.0094	0.0044	0.0094	0.0017	0.0160	0.0014	0.0013	0.0067	0.0238
449	0.0074	0.0031	0.0010	0.0094	0.0046	0.0096	0.0017	0.0164	0.0013	0.0012	0.0071	0.0243
456	0.0073	0.0031	0.0011	0.0094	0.0048	0.0095	0.0018	0.0163	0.0013	0.0012	0.0072	0.0241
463	0.0082	0.0034	0.0013	0.0107	0.0058	0.0104	0.0022	0.0185	0.0015	0.0015	0.0081	0.0279
470	0.0096	0.0039	0.0017	0.0127	0.0076	0.0116	0.0031	0.0220	0.0019	0.0020	0.0091	0.0331
477	0.0118	0.0048	0.0023	0.0159	0.0104	0.0135	0.0045	0.0275	0.0024	0.0029	0.0103	0.0418
484	0.0138	0.0056	0.0027	0.0193	0.0139	0.0145	0.0064	0.0335	0.0028	0.0036	0.0106	0.0514
491	0.0154	0.0064	0.0033	0.0222	0.0176	0.0145	0.0092	0.0389	0.0034	0.0046	0.0100	0.0596
498	0.0156	0.0065	0.0034	0.0236	0.0200	0.0132	0.0124	0.0415	0.0037	0.0051	0.0084	0.0638
505	0.0153	0.0066	0.0034	0.0244	0.0215	0.0118	0.0161	0.0429	0.0039	0.0055	0.0069	0.0657
512	0.0148	0.0065	0.0036	0.0251	0.0219	0.0105	0.0199	0.0441	0.0042	0.0061	0.0058	0.0677
519	0.0140	0.0063	0.0035	0.0257	0.0209	0.0093	0.0229	0.0453	0.0045	0.0072	0.0048	0.0697
526	0.0136	0.0064	0.0037	0.0267	0.0191	0.0084	0.0248	0.0470	0.0049	0.0091	0.0043	0.0717
533	0.0133	0.0065	0.0039	0.0276	0.0176	0.0078	0.0257	0.0488	0.0051	0.0112	0.0040	0.0740
540	0.0134	0.0067	0.0039	0.0286	0.0174	0.0074	0.0259	0.0504	0.0053	0.0128	0.0038	0.0766
547	0.0135	0.0070	0.0040	0.0297	0.0183	0.0072	0.0255	0.0524	0.0056	0.0143	0.0037	0.0793
554	0.0136	0.0075	0.0043	0.0309	0.0198	0.0072	0.0248	0.0544	0.0062	0.0164	0.0038	0.0822
561	0.0131	0.0079	0.0043	0.0318	0.0201	0.0069	0.0233	0.0557	0.0065	0.0191	0.0037	0.0843
568	0.0126	0.0084	0.0046	0.0325	0.0204	0.0068	0.0217	0.0568	0.0072	0.0231	0.0036	0.0865
575	0.0133	0.0102	0.0057	0.0358	0.0241	0.0073	0.0215	0.0628	0.0087	0.0308	0.0041	0.0941
582	0.0132	0.0135	0.0069	0.0375	0.0294	0.0074	0.0196	0.0652	0.0100	0.0396	0.0041	0.0981
589	0.0133	0.0194	0.0088	0.0378	0.0358	0.0074	0.0170	0.0659	0.0111	0.0479	0.0041	0.0998
596	0.0141	0.0304	0.0135	0.0410	0.0458	0.0081	0.0156	0.0709	0.0129	0.0596	0.0045	0.1073
603	0.0162	0.0475	0.0234	0.0481	0.0598	0.0095	0.0158	0.0833	0.0157	0.0758	0.0051	0.1224
610	0.0168	0.0614	0.0364	0.0513	0.0683	0.0103	0.0152	0.0887	0.0174	0.0838	0.0055	0.1306

Table 8.10: *Measured radiance values of an X-Rite Mini ColorChecker (#13 - #24) for a wavelength range 400–610 nm, measured with a spectroradiometer.*

Color patches												
Wave-length	#1	#2	#3	#4	#5	#6	#7	#8	#9	#10	#11	#12
617	0.0164	0.0691	0.0503	0.0508	0.0713	0.0101	0.0141	0.0881	0.0177	0.0843	0.0056	0.1327
624	0.0163	0.0748	0.0636	0.0510	0.0746	0.0103	0.0137	0.0886	0.0183	0.0850	0.0056	0.1357
631	0.0165	0.0797	0.0748	0.0521	0.0788	0.0108	0.0137	0.0904	0.0197	0.0865	0.0059	0.1401
638	0.0173	0.0836	0.0831	0.0530	0.0833	0.0116	0.0138	0.0928	0.0214	0.0883	0.0062	0.1447
645	0.0185	0.0875	0.0900	0.0550	0.0891	0.0128	0.0140	0.0959	0.0233	0.0909	0.0067	0.1508
652	0.0197	0.0905	0.0945	0.0560	0.0946	0.0140	0.0141	0.0984	0.0249	0.0923	0.0069	0.1556
659	0.0213	0.0935	0.0991	0.0581	0.1011	0.0158	0.0146	0.1019	0.0268	0.0950	0.0074	0.1617
666	0.0227	0.0965	0.1027	0.0593	0.1076	0.0179	0.0153	0.1045	0.0281	0.0977	0.0078	0.1663
673	0.0240	0.1000	0.1074	0.0615	0.1158	0.0205	0.0167	0.1087	0.0293	0.1027	0.0084	0.1733
680	0.0240	0.1005	0.1080	0.0621	0.1199	0.0231	0.0181	0.1089	0.0288	0.1050	0.0090	0.1742
687	0.0241	0.1022	0.1105	0.0630	0.1263	0.0264	0.0191	0.1106	0.0284	0.1091	0.0092	0.1782
694	0.0238	0.1044	0.1134	0.0638	0.1330	0.0306	0.0205	0.1128	0.0283	0.1136	0.0097	0.1823
701	0.0237	0.1062	0.1159	0.0650	0.1408	0.0359	0.0219	0.1148	0.0289	0.1182	0.0106	0.1853
708	0.0230	0.1075	0.1180	0.0654	0.1464	0.0420	0.0228	0.1162	0.0297	0.1222	0.0114	0.1885
715	0.0229	0.1089	0.1198	0.0660	0.1527	0.0483	0.0224	0.1173	0.0307	0.1247	0.0122	0.1912
722	0.0242	0.1083	0.1193	0.0658	0.1551	0.0551	0.0223	0.1162	0.0324	0.1246	0.0138	0.1909
729	0.0258	0.1081	0.1193	0.0657	0.1573	0.0625	0.0217	0.1154	0.0338	0.1248	0.0154	0.1905
736	0.0280	0.1088	0.1208	0.0660	0.1604	0.0697	0.0222	0.1168	0.0364	0.1265	0.0174	0.1929
743	0.0318	0.1090	0.1212	0.0656	0.1613	0.0764	0.0236	0.1163	0.0403	0.1289	0.0211	0.1931
750	0.0354	0.1070	0.1182	0.0638	0.1586	0.0804	0.0250	0.1138	0.0434	0.1285	0.0249	0.1889
757	0.0428	0.1112	0.1241	0.0668	0.1664	0.0888	0.0291	0.1180	0.0512	0.1369	0.0332	0.1975
764	0.0490	0.1163	0.1297	0.0694	0.1742	0.0967	0.0324	0.1234	0.0587	0.1453	0.0421	0.2062
771	0.0498	0.1115	0.1256	0.0666	0.1681	0.0962	0.0326	0.1185	0.0603	0.1420	0.0474	0.1991
778	0.0477	0.1042	0.1174	0.0620	0.1569	0.0915	0.0309	0.1104	0.0594	0.1336	0.0508	0.1855
785	0.0473	0.1021	0.1154	0.0607	0.1543	0.0918	0.0305	0.1080	0.0603	0.1328	0.0562	0.1819
792	0.0466	0.0988	0.1120	0.0593	0.1498	0.0907	0.0311	0.1047	0.0603	0.1304	0.0611	0.1759
799	0.0451	0.0956	0.1085	0.0567	0.1441	0.0878	0.0322	0.1006	0.0591	0.1278	0.0647	0.1703
806	0.0432	0.0921	0.1054	0.0542	0.1399	0.0861	0.0348	0.0975	0.0571	0.1267	0.0670	0.1647
813	0.0426	0.0901	0.1026	0.0532	0.1364	0.0836	0.0392	0.0951	0.0557	0.1241	0.0688	0.1601
820	0.0415	0.0874	0.0997	0.0519	0.1311	0.0826	0.0448	0.0921	0.0536	0.1221	0.0706	0.1558
827	0.0387	0.0828	0.0945	0.0489	0.1254	0.0786	0.0485	0.0873	0.0506	0.1168	0.0685	0.1477
834	0.0374	0.0793	0.0910	0.0470	0.1202	0.0760	0.0530	0.0833	0.0487	0.1132	0.0682	0.1415
841	0.0361	0.0760	0.0879	0.0444	0.1156	0.0733	0.0581	0.0799	0.0462	0.1091	0.0672	0.1352
848	0.0342	0.0728	0.0833	0.0427	0.1096	0.0710	0.0619	0.0756	0.0441	0.1045	0.0658	0.1280
855	0.0323	0.0682	0.0793	0.0400	0.1033	0.0678	0.0634	0.0718	0.0418	0.0993	0.0632	0.1216

Table 8.11: *Measured radiance values of an X-Rite Mini ColorChecker (#13 - #24) for a wavelength range 617–855 nm, measured with a spectroradiometer.*

Color patches												
Wave-length	#1	#2	#3	#4	#5	#6	#7	#8	#9	#10	#11	#12
862	0.0308	0.0646	0.0750	0.0378	0.0986	0.0646	0.0646	0.0677	0.0395	0.0945	0.0613	0.1153
869	0.0290	0.0611	0.0714	0.0356	0.0930	0.0620	0.0647	0.0643	0.0372	0.0892	0.0587	0.1092
876	0.0268	0.0566	0.0660	0.0328	0.0862	0.0580	0.0629	0.0593	0.0347	0.0832	0.0556	0.1018
883	0.0270	0.0561	0.0650	0.0327	0.0848	0.0573	0.0641	0.0583	0.0350	0.0819	0.0556	0.0997
890	0.0307	0.0648	0.0754	0.0374	0.0985	0.0676	0.0773	0.0673	0.0407	0.0956	0.0654	0.1158
897	0.0321	0.0676	0.0789	0.0392	0.1027	0.0718	0.0828	0.0706	0.0433	0.0997	0.0692	0.1214
904	0.0258	0.0546	0.0638	0.0321	0.0835	0.0585	0.0681	0.0565	0.0354	0.0808	0.0571	0.0978
911	0.0211	0.0454	0.0528	0.0261	0.0696	0.0493	0.0573	0.0478	0.0296	0.0668	0.0473	0.0815
918	0.0193	0.0407	0.0477	0.0238	0.0617	0.0447	0.0515	0.0426	0.0274	0.0606	0.0434	0.0731
925	0.0173	0.0361	0.0421	0.0207	0.0553	0.0404	0.0468	0.0375	0.0250	0.0538	0.0387	0.0648
932	0.0153	0.0315	0.0372	0.0187	0.0482	0.0359	0.0413	0.0326	0.0220	0.0479	0.0345	0.0564
939	0.0134	0.0267	0.0312	0.0162	0.0403	0.0301	0.0340	0.0278	0.0193	0.0395	0.0294	0.0464
946	0.0075	0.0167	0.0191	0.0094	0.0249	0.0186	0.0220	0.0171	0.0123	0.0248	0.0184	0.0297
953	0.0078	0.0159	0.0188	0.0094	0.0246	0.0190	0.0208	0.0168	0.0119	0.0238	0.0184	0.0284
960	0.0077	0.0166	0.0200	0.0092	0.0257	0.0194	0.0221	0.0177	0.0129	0.0252	0.0187	0.0305
967	0.0071	0.0159	0.0190	0.0086	0.0248	0.0194	0.0215	0.0163	0.0123	0.0240	0.0184	0.0292
974	0.0065	0.0151	0.0185	0.0087	0.0239	0.0178	0.0205	0.0157	0.0123	0.0224	0.0177	0.0274
981	0.0060	0.0134	0.0160	0.0072	0.0208	0.0159	0.0182	0.0139	0.0109	0.0198	0.0158	0.0241
988	0.0048	0.0120	0.0141	0.0063	0.0185	0.0146	0.0162	0.0120	0.0099	0.0178	0.0133	0.0216
995	0.0031	0.0087	0.0111	0.0045	0.0145	0.0115	0.0130	0.0094	0.0078	0.0142	0.0111	0.0172
1002	0.0023	0.0074	0.0088	0.0036	0.0121	0.0095	0.0108	0.0074	0.0059	0.0117	0.0091	0.0141
1009	0.0031	0.0070	0.0086	0.0040	0.0112	0.0090	0.0097	0.0073	0.0060	0.0110	0.0082	0.0125
1016	0.0026	0.0059	0.0071	0.0035	0.0093	0.0076	0.0087	0.0065	0.0059	0.0092	0.0073	0.0112
1023	0.0037	0.0061	0.0076	0.0037	0.0083	0.0072	0.0074	0.0061	0.0054	0.0087	0.0068	0.0102
1030	0.0003	0.0027	0.0037	0.0008	0.0042	0.0032	0.0035	0.0027	0.0015	0.0042	0.0035	0.0056
1037	0.0000	0.0000	0.0000	0.0000	0.0000	0.0000	0.0000	0.0000	0.0000	0.0000	0.0000	0.0000
1044	0.0000	0.0000	0.0000	0.0000	0.0000	0.0000	0.0000	0.0000	0.0000	0.0000	0.0000	0.0000
1051	0.0000	0.0000	0.0000	0.0000	0.0000	0.0000	0.0000	0.0000	0.0000	0.0000	0.0000	0.0000
1058	0.0000	0.0000	0.0000	0.0000	0.0000	0.0000	0.0000	0.0000	0.0000	0.0000	0.0000	0.0000
1065	0.0000	0.0000	0.0000	0.0000	0.0000	0.0000	0.0000	0.0000	0.0000	0.0000	0.0000	0.0000
1072	0.0000	0.0000	0.0000	0.0000	0.0000	0.0000	0.0000	0.0000	0.0000	0.0000	0.0000	0.0000
1079	0.0000	0.0000	0.0000	0.0000	0.0000	0.0000	0.0000	0.0000	0.0000	0.0000	0.0000	0.0000
1086	0.0000	0.0000	0.0000	0.0000	0.0000	0.0000	0.0000	0.0000	0.0000	0.0000	0.0000	0.0000
1093	0.0000	0.0000	0.0000	0.0000	0.0000	0.0000	0.0000	0.0000	0.0000	0.0000	0.0000	0.0000
1100	0.0000	0.0000	0.0000	0.0000	0.0000	0.0000	0.0000	0.0000	0.0000	0.0000	0.0000	0.0000

Table 8.12: *Measured radiance values of an X-Rite Mini ColorChecker (#13 - #24) for a wavelength range 862–1100 nm, measured with a spectroradiometer.*

Appendix B. Hyperspectral Image

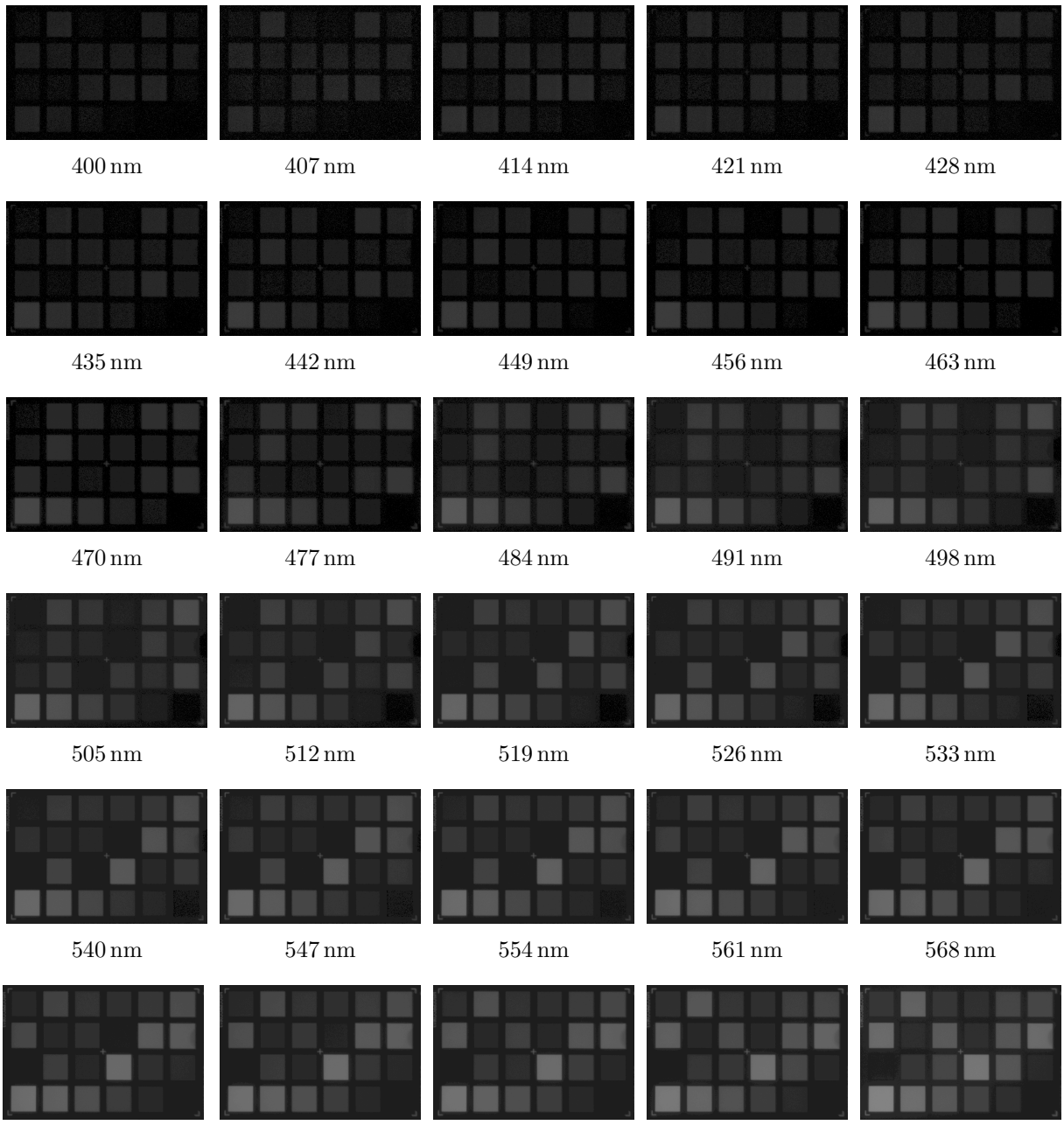

Figure 9.1: *Hyperspectral image of an X-Rite Mini ColorChecker (1/3)*

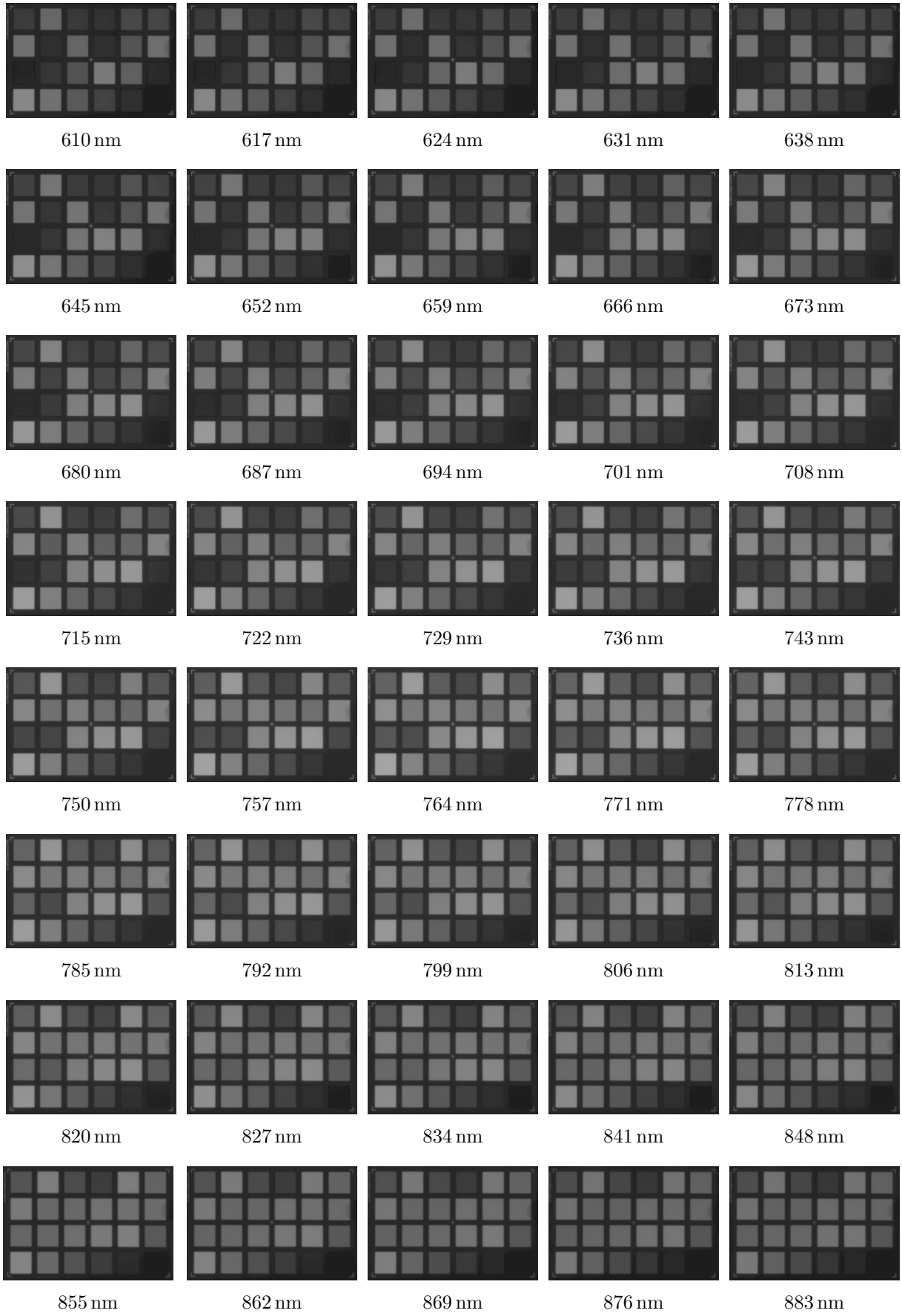

Figure 9.2: *Hyperspectral image of an X-Rite Mini ColorChecker (2/3)*

Figure 9.3: *Hyperspectral image of an X-Rite Mini ColorChecker (3/3) and a converted sRGB image*

References

[1] Manoj Aggarwal and Narendra Ahuja. Split aperture imaging for high dynamic range. *International Journal of Computer Vision*, 58(1):7–17, 2004.

[2] Toygar Akgun, Yucel Altunbasak, and Russell M Mersereau. Super-resolution reconstruction of hyperspectral images. *Image Processing, IEEE Transactions on*, 14(11):1860–1875, 2005.

[3] Michael Attas, Edward Cloutis, Catherine Collins, Douglas Goltz, Claudine Majzels, James R Mansfield, and Henry H Mantsch. Near-infrared spectroscopic imaging in art conservation: investigation of drawing constituents. *Journal of Cultural Heritage*, 4(2):127–136, 2003.

[4] Johannes Brauers, Nils Schulte, and Til Aach. Modeling and compensation of geometric distortions of multispectral cameras with optical bandpass filter wheels. In *15th European Signal Processing Conference*, volume 15, pages 1902–1906, 2007.

[5] G. Buchsbaum. A Spatial Processor Model for Object Colour Perception. *J. the Franklin Institute*, 310(1):1–26, 1980.

[6] P. D. Burns and D. Williams. Refined slanted-edge measurements for practical camera and scanner testing. In *Proc. PICS Conf.*, pages 191–195. IS&T, 2002.

[7] Peter D Burns. Slanted-edge mtf for digital camera and scanner analysis. In *Proc. IS&T PICS Conference*, pages 135–138. IS&T, 2000.

[8] CIE. Colorimetry. CIE Pub. 15.2, Commission Internationale de l'Eclairage (CIE), Vienna, 1986.

[9] Hao Du, Xin Tong, Xun Cao, and Stephen Lin. A prism-based system for multispectral video acquisition. In *Computer Vision, 2009 IEEE 12th International Conference on*, pages 175–182. IEEE, 2009.

[10] Mark D Fairchild. *Color Appearance Models*. John Wiley & Sons, 2013.

[11] Martin A Fischler and Robert C Bolles. Random sample consensus: a paradigm for model fitting with applications to image analysis and automated cartography. *Communications of the ACM*, 24(6):381–395, 1981.

[12] Nahum Gat. Imaging spectroscopy using tunable filters: a review. In *AeroSense 2000*, pages 50–64. International Society for Optics and Photonics, 2000.

[13] Ralf Habel, Michael Kudenov, and Michael Wimmer. Practical spectral photography. In *Computer Graphics Forum*, volume 31, pages 449–458. Wiley Online Library, 2012.

[14] Jon Y Hardeberg, Francis Schmitt, and Hans Brettel. Multispectral color image capture using a liquid crystal tunable filter. *Optical engineering*, 41(10):2532–2548, 2002.

[15] Andrew R Harvey, Joanne Lawlor, Andrew I McNaught, John W Williams, and David W Fletcher-Holmes. Hyperspectral imaging for the detection of retinal disease. In *International Symposium on Optical Science and Technology*, pages 325–335. International Society for Optics and Photonics, 2002.

[16] Eugene Hecht and A Zajac. Optics addison-wesley. *Reading, Mass*, pages 301–305, 1974.

[17] Gudrun Hoye and Andrei Fridman. Mixel camera—-a new push-broom camera concept for high spatial resolution keystone-free hyperspectral imaging. *Optics express*, 21(9):11057–11077, 2013.

[18] Jenoptik, Inc. Jenoptik, Inc. http://jenoptik-inc.com.

[19] Min H. Kim, Todd Alan Harvey, David S. Kittle, Holly Rushmeier, Julie Dorsey, Richard O. Prum, and David J. Brady. 3d imaging spectroscopy for measuring hyperspectral patterns on solid objects. *ACM Transactions on Graphics (Proc. SIGGRAPH 2012)*, 31(4):38:1–11, 2012.

[20] Min H. Kim and Holly Rushmeier. Radiometric characterization of spectral imaging for textual pigment identification. In *Proc. International Symposium on Virtual Reality, Archaeology and Cultural Heritage (VAST 2011)*, pages 57–64, Tuscany, Italy, 2011. Eurographics.

[21] Guolan Lu, Luma Halig, Dongsheng Wang, Xulei Qin, Zhuo Georgia Chen, and Baowei Fei. Spectral-spatial classification for noninvasive cancer detection using hyperspectral imaging. *Journal of biomedical optics*, 19(10):106004–106004, 2014.

[22] Renfu Lu. Detection of bruises on apples using near-infrared hyperspectral imaging. *Transactions-American Society of Agricultural Engineers*, 46(2):523–530, 2003.

[23] Lucas Digital Ltd. OpenEXR. http://www.openexr.com/, 2009.

[24] Alamin Mansouri, Alexandra Lathuiliere, Franck S Marzani, Yvon Voisin, and Pierre Gouton. Toward a 3d multispectral scanner: an application to multimedia. *MultiMedia, IEEE*, 14(1):40–47, 2007.

[25] Morgan McGuire, Wojciech Matusik, Hanspeter Pfister, Billy Chen, John F Hughes, and Shree K Nayar. Optical splitting trees for high-precision monocular imaging. *Computer Graphics and Applications, IEEE*, 27(2):32–42, 2007.

[26] Pantazis Mouroulis, Robert O Green, and Thomas G Chrien. Design of pushbroom imaging spectrometers for optimum recovery of spectroscopic and spatial information. *Applied Optics*, 39(13):2210–2220, 2000.

[27] Hamed Hamid Muhammed. Hyperspectral crop reflectance data for characterising and estimating fungal disease severity in wheat. *Biosystems Engineering*, 91(1):9–20, 2005.

[28] Mary Nielsen and Michael Stokes. The creation of the sRGB ICC Profile. In *Proc. Color Imaging Conf.*, pages 253–257. IS&T, 1998.

[29] OpenCV Developers Team. OpenCV. http://opencv.org.

[30] PerkinElmer Inc. PerkinElmer Inc. http://www.perkinelmer.com.

[31] Konstantinos Rapantzikos and Costas Balas. Hyperspectral imaging: potential in non-destructive analysis of palimpsests. In *Image Processing, 2005. ICIP 2005. IEEE International Conference on*, volume 2, pages II–618. IEEE, 2005.

[32] MA Sid-Ahmed and Mohamed T Boraie. Dual camera calibration for 3-D machine vision metrology. *IEEE Transactions on Instrumentation and Measurement (TIM)*, 39(3):512–516, 1990.

[33] Michael D Tocci, Chris Kiser, Nora Tocci, and Pradeep Sen. A versatile hdr video production system. In *ACM Transactions on Graphics (TOG)*, volume 30, page 41. ACM, 2011.

[34] Fabrizio Vagni. Survey of hyperspectral and multispectral imaging technologies. 2007.

[35] Don Williams and Peter D Burns. Low-frequency MTF estimation for digital imaging devices using slanted-edge analysis. In *Proc. IS&T/SPIE Electronic Imaging*, pages 93–101, 2003.

[36] Lawrence B Wolff. Polarization camera for computer vision with a beam splitter. *JOSA A*, 11(11):2935–2945, 1994.

[37] Zemax, LLC. Zemax. http://www.zemax.com.

[38] Xujie Zhang, Tamar Kashti, Dror Kella, Tal Frank, Doron Shaked, Robert Ulichney, Mani Fischer, and Jan P Allebach. Measuring the modulation transfer function of image capture devices: what do the numbers really mean? In *Proc. IS&T/SPIE Electronic Imaging*, pages 829307–829307, 2012.

Summary

Building a Two-Way Hyperspectral Imaging System with Liquid Crystal Tunable Filters

가변적 액정 필터들은 특정 영역의 빛을 선택적으로 통과시킴에 있어 빠르고 진동이 없는 방법을 제공하기 때문에 다분광 이미징 시스템 또는 초분광 이미징 시스템 구축에 널리 사용되어왔다. 그러나, 각 필터의 스펙트럼 범위는 가시광선 영역 또는 근적외선 영역 같은 특정 범위로 제한되어 있다. 그러므로 일반적인 분광 이미징 시스템에서는 가시광선 영역, 근적외선 영역과 같이 목표로 하는 스펙트럼 영역 하나만을 선택해야 한다. 편광 광학 소자의 특성으로 인해, 다수의 가변적 필터를 사용하는 이미징 시스템은 거의 구현되지 않았다. 이 논문에서 우리는 가변적 액정 필터와 간단한 두 방향 초분광 이미징 시스템을 구축한 경험을 공유하고자 한다. 이 시스템은 가시광선 영역에서부터 근적외선 영역까지 (400 – 1100 nm 영역에서 7 nm 간격) 연속적으로 초분광 복사 휘도를 캡처하는데, 이것은 우리가 일반적으로 사용하는 RGB 카메라에 비해 2.3 배 넓은 영역에서 34 배 더 많은 채널을 제공하는 것이다. 우리가 여러개의 가변적 필터와 편광기기를 사용하여 이미징 시스템의 스펙트럼 범위를 확장한 방법과, 각 파장의 분광 이미지 채널을 어파인 기반 접근을 통하여 정렬한 방법에 대해 보고한다.

감 사 의 글

석사 학위 논문과 유학, 그리고 결혼이라는 인륜지대사를 동시에 준비하게 되는 바람에, 도움을 주신 분들이 없었더라면 세 마리 토끼를 다 놓쳤을 것 같습니다. 먼저 지금의 제가 있기까지 아낌없이 도와주고, 믿어주고, 기도해주고, 사랑해주신 부모님께 감사의 인사를 올립니다. 항상 에너지가 넘치는 사랑하는 동생 이슬이에게도 이 자리를 빌어 감사를 표합니다. 이제 한 가정을 이루고 평생을 같이 살아가게 될 윤아에게는 제 결정을 믿고 따라주고, 언제나 사랑과 격려를 준 것에 대해 큰 고마움과 사랑을 전하고 싶습니다. 제 2의 부모님이 되어주실 장인 장모님께도 감사의 말씀을 드립니다.

우리 VCLAB 식구들에게도 고마움을 표현하고자 합니다. 어릴 때부터 알던 사이같이 친근한 길주형, 실력 있는 최고참이자 저를 VCLAB으로 이끌어준 인창이, 듬직하고 꼼꼼한 영범이, 키 크고 잘생긴데다가 사진도 잘 찍는 인철이, 아프리카 BJ급 입담을 자랑하는 주호, 번득이는 통찰력을 가진 승환이, 그리고 조용한 광학 에이스 석준이, 모두가 이 논문을 쓰는 과정에 도움과 조언을 마다하지 않았습니다. 이에 대해 깊은 감사를 드리며, 모두에게 행복한 일이 가득하기를 바라는 바입니다.

그 외에도 자랑스런 경남과학고 동문들, 특히 김병수군과 김준호군, 그리고 10년 째 우정을 나누고 있는 해동검도회 동기들과 두 분의 유치원 선배님들께도 감사의 말씀을 드립니다.

물론 이 논문을 작성함에 있어 누구보다도 큰 도움을 주신 분은 지도교수님이신 김민혁 교수님일 것입니다. 여러모로 부족함이 많은 저를 이끌어주셨고, 학문적인 부분은 물론이거니와 인간적인 부분에서도 제게 큰 귀감이 되어주셨습니다. 교수님의 제자가 될 수 있었던 것을 큰 축복이자 영광으로 생각하며, 그간 베풀어주신 지도와 배려에 깊은 감사와 존경의 인사를 올립니다.

이 밖에 언급하지 못한 분들에게도 감사한 마음을 전하며, 건강과 행복이 함께 하길 바랍니다.

이 력 서

이 름 : 이 해 봄

생 년 월 일 : 1988년 2월 3일

E-mail 주 소 : haebomlee@gmail.com

학 력

2003. 3. – 2005. 2. 경남과학고등학교

2005. 3. – 2009. 2. KAIST 전산학과 (B.S.)

경 력

2009. 3. – 2013. 4. (주)컴투스 선임연구원

2013. 9. – 2015. 6. 한국과학기술원 전산학과 일반조교

학 회 활 동

1. **Haebom Lee** and Min H. Kim, *Building a Two-Way Hyperspectral Imaging System with Liquid Crystal Tunable Filters*, International Conference of Image and Signal Processing (ICISP), June., 2014, **Oral presentation**.

연 구 업 적

1. **Haebom Lee** and Min H. Kim, *Building a Two-Way Hyperspectral Imaging System with Liquid Crystal Tunable Filters*, Lecture Notes in Computer Science (LNCS) Vol. 8509, June 2014, pp. 26-34.